

RIS-Empowered OTFS Modulation With Faster-than-Nyquist Signaling in High-Mobility Wireless Communications

Chaorong Zhang, Benjamin K. Ng, Hui Xu, Chan-Tong Lam, and Halim Yanikomeroglu,

Abstract—Faster-than-Nyquist (FTN) signaling offers a promising path to enhance the spectral efficiency (SE) of orthogonal time frequency space (OTFS) modulation in high-mobility scenarios. However, the inherent non-orthogonal pulse shaping induces severe structured interference and colored noise, leading to reliability degradation and error floors. This paper proposes a reconfigurable intelligent surface (RIS)-empowered OTFS-FTN framework, demonstrating that the RIS acts as a critical enabler rather than a generic SNR booster. By strategically configuring RIS phases, we reshape the cascaded delay-Doppler (DD) channel to mitigate FTN-induced impairments, thereby enhancing reliability and relaxing power amplifier (PA) back-off constraints. We establish a unified DD-domain model explicitly accounting for FTN-induced colored noise and derive analytical expressions for the average frame error rate (AFER) upper bound, SE, peak-to-average power ratio (PAPR), and input back-off (IBO). Moreover, a low-complexity RIS phase design is proposed, with quantified computational and control overheads. Extensive simulations against comprehensive baselines, including Nyquist OTFS and power-compensated benchmarks, validate that the proposed framework achieves a superior SE-reliability-IBO trade-off. Results show up to around 10 dB reduction in required SNR for equivalent SE and AFER, confirming gains that cannot be replicated by simply optimizing simpler systems.

Index Terms—Orthogonal Time Frequency Space, Faster-than-Nyquist, Reconfigurable Intelligent Surface, spectral efficiency

I. INTRODUCTION

A. Orthogonal Time Frequency Space

As emerging technologies like the Internet of Things (IoT), Vehicle-to-Everything (V2X), and low-Earth-orbit (LEO) satellite communications continue to advance, there is growing focus on improving the quality of mobile wireless communications [1]-[3]. However, traditional wireless schemes such as the Orthogonal Frequency Division Multiplexing (OFDM) perform poorly in high-mobility scenarios, particularly in terms of error performance, mainly because they lack strong robustness against delay and Doppler effects [4]. In contrast, the Orthogonal Time Frequency Space (OTFS) modulation offers a better solution to this challenge. OTFS is an emerging two-dimensional modulation scheme that represents information symbols in the delay-Doppler (DD) domain, rather than in the conventional time-frequency (TF) domain [5]-[6]. By exploiting the quasi-static nature of wireless channels in the DD

domain, OTFS achieves a more compact and stable channel representation, enabling all information symbols to experience the full TF diversity of the channel. This property makes OTFS particularly robust against severe Doppler spread and delay dispersion, which are common in high-mobility and frequency-selective environments such as high-speed trains, vehicular communications, and LEO satellite links [7]-[8]. Despite this, there remains significant potential to further enhance OTFS's error performance and spectral efficiency under time-varying channel conditions. **Motivated by this, enhancing OTFS in high-mobility regimes calls for jointly improving spectral efficiency and reliability, which naturally leads to combining FTN signaling with controllable propagation technologies under a unified design and analysis framework.**

B. Faster-than-Nyquist

As one of the famous high-efficiency techniques in wireless communications, the faster-than-Nyquist (FTN) signaling is a promising transmission technique that intentionally compresses the symbol spacing below the limited Nyquist rate in the time domain, thereby increasing the data rate within a given bandwidth [9]-[10]. By introducing a controllable and acceptable level of intentional inter-symbol interference (ISI), FTN enables more symbols to be transmitted over the same spectral resources, effectively enhancing spectral efficiency without expanding the occupied bandwidth. Several state-of-the-art works show that a carefully designed FTN system can achieve higher data rates without a proportional degradation in error performance, provided that advanced detection or equalization algorithms are employed [11]-[15]. This property makes FTN particularly attractive for modern and future wireless communication scenarios where spectral resources are scarce, such as high-capacity terrestrial wireless networks, IoT applications, and next-generation satellite systems. Moreover, FTN can be flexibly combined with emerging modulation techniques like OTFS, leveraging the DD domain processing to mitigate ISI and improve robustness in high-mobility environments. FTN signaling improves the SE of OTFS by intentionally accelerating the symbol rate. Yet, the resulting non-orthogonal pulse shaping produces structured interference and colored noise after matched filtering and sampling, which fundamentally differs from the white-noise assumption in conventional OTFS receivers. **However, the effective DD-domain channel becomes less sparse and the receiver must cope with both intensified inter-symbol coupling**

(Corresponding author: Benjamin K. Ng.) Chaorong Zhang, Benjamin K. Ng, Hui Xu, and Chan-Tong Lam are with the Faculty of Applied Sciences, Macao Polytechnic University, Macao SAR, China. Halim Yanikomeroglu is with System and Computer Engineering Department, Carleton University, Ottawa, ON K1S 5B6, Canada.

and noise correlation with FTN application, potentially leading to error floors and sharply increased detection complexity.

C. Reconfigurable Intelligent Surface

Thus, a novel and popular wireless technique called the Reconfigurable intelligent surfaces (RIS) is introduced in our work. RIS has recently emerged as a promising enabling technology for beyond fifth-generation (B5G) and sixth-generation (6G) wireless communication systems. An RIS typically consists of a two-dimensional (2D) planar array of reconfigurable reflection elements each fabricated from engineered materials capable of manipulating incident electromagnetic waves in a programmable manner [16]. Each reflection element can be individually controlled by an intelligent controller or chip, which receives configuration instructions from the transmitter and adjusts the phase shifts of the reflected signals accordingly [17]. This unique capability enables RIS to reshape the wireless propagation environment by steering the reflected beams toward desired directions, thereby extending coverage, enhancing received signal power, and improving link reliability. Unlike conventional active relays such as unmanned aerial vehicles or vehicular relays, RIS operates without radio-frequency (RF) chains, power amplifiers, or active signal regeneration [18]. As a result, it can achieve high beamforming gains with minimal power consumption, a feature commonly referred to as passive beamforming [19]-[20]. Through intelligent phase shift optimization, RIS can enhance the signal-to-noise ratio (SNR) at the receiver while incurring negligible additional energy cost, making it highly attractive for energy-efficient wireless communications. Since FTN causes degradation in bit-error rate (BER) performance and OTFS still fails to achieve sufficiently satisfactory performance in high-mobility scenarios, RIS can be considered to address these issues. Despite its robustness, RIS-OTFS faces a fundamental SE ceiling imposed by the Nyquist criterion. Although high-order modulations can improve SE, they degrade severely in harsh fading channels. Consequently, existing systems suffer from a rigid robustness-efficiency trade-off, preventing the simultaneous achievement of high data rates and reliable transmission. In our work, RIS provides benefits beyond simple SNR enhancement. When FTN-aided interference dominates, only increasing transmit power is inefficient and limited by power amplifiers (PA) back-off (IBO) and peak-to-average power ratio (PAPR)-induced nonlinearity. By configuring phases, RIS can reshape the cascaded channel to improve post-equalization reliability under FTN. This reduces the required transmit power and expands the feasible IBO region for a target AFER and SE, demonstrating a non-trivial synergy between RIS and OTFS-FTN beyond a mere combination of two.

D. Related Works

Recently, several studies investigate the RIS-assisted OTFS (RIS-OTFS) and FTN-assisted OTFS (FTN-OTFS) schemes. On the one hand, the pure RIS-OTFS schemes are first proposed and analyzed in [21]-[25], where RIS significantly improves the BER performance of OTFS systems. In addition, fundamental aspects such as the input-output relationship,

RIS phase adjustment design, multiple-input multiple-output (MIMO) system modeling, and channel estimation are thoroughly discussed in these works. However, further theoretical investigation of RIS-OTFS is still required, particularly in terms of error performance, spectral efficiency, and the power fluctuation characteristics of modulated signals, in order to provide deeper insights for practical applications. Later, [26] proposes a novel index modulation-aided RIS-OTFS scheme to enhance spectral efficiency, but it further increases the detection complexity that is already high in OTFS system. As another high-efficiency technology, FTN serves as a better alternative to index modulation, offering lower detection complexity while supporting higher data rates. On the other hand, various FTN-OTFS schemes are proposed and examined in [27]-[30]. While these schemes improve the spectral efficiency of OTFS systems, they often suffer from degraded BER performance. In particular, when frequency compression is applied, as in [29]-[30], the BER performance further deteriorates due to the increased ISI. Plus, [31] demonstrates a low-complexity transceiver for OTFS-FTN that applies Reverse Cuthill-McKee reordering and Cholesky factorization to the sparse channel matrix. This reduces complexity from cubic to near-linear in frame size, providing a feasible path to deploy the proposed system at scale. Overall, both of these fields lack sufficient literature to provide a stronger theoretical foundation and more insights, leaving a research gap and potential improvement among the RIS, FTN, and OTFS.

E. Contributions

OTFS mitigates Doppler spread in high-mobility scenarios but is limited to Nyquist-rate SE. FTN surpasses this limit via compressed symbol spacing, yet introduces severe ISI that degrades reliability. To address this, we employ RIS. Its passive beamforming gain effectively offsets the SNR penalty incurred by FTN. This synergy supports aggressive FTN compression, unlocking high SE without compromising the reliability of OTFS in challenging channels, thereby overcoming the traditional mobility-SE trade-off. In light of the above works and motivated aforementioned challenges in reliability and spectral efficiency, a novel wireless scheme called the RIS-empowered OTFS modulation with FTN signaling (RIS-OTFS-FTN) scheme is proposed and investigated in this paper. Main contributions of our work are briefly summarized as

- **The RIS-OTFS-FTN scheme is firstly proposed and comprehensively investigated in this paper.** The input-output relationship in the DD domain is provided, which explicitly characterizes the joint effects of RIS-induced passive beamforming, FTN-induced intentional ISI, and the inherent delay-Doppler channel dynamics. This unified mathematical framework lays the foundation for systematic performance evaluation and facilitates the development of optimized signal processing.
- **We perform a theoretical analysis of the average frame error rate (AFER) for the proposed RIS-OTFS-FTN scheme.** By leveraging the derived DD-domain model, we obtain closed-form FER expressions that capture the influence of key system parameters. These analytical

results not only reveal insightful trade-offs between spectral efficiency and reliability but also serve as valuable guidelines for system design in high-mobility scenarios.

- **Since no existing studies on RIS-OTFS systems have provided relevant analytical performance results**, we present theoretical formulations for evaluating spectral efficiency, PAPR, and other aspects of analytical performance. These formulations offer a theoretical foundation and framework with valuable insights, supporting practical applications and further system extensions.
- **A tailored RIS phase adjustment strategy that optimizes the discrete phase shifts of individual reflection elements based on the DD channel state information is designed.** This design aligns reflected signal components constructively at receiver, thus maximizing the effective channel gain. The proposed method accounts for practical hardware constraints by employing quantized phase control, while still achieving near-optimal performance.
- **We present extensive Monte Carlo simulations and theoretical results, along with a series of in-depth performance insights**, including the interplay among frame error rate (FER), spectral efficiency, PAPR, complementary cumulative distribution function (CCDF), IBO, and BER in high-mobility scenarios. Furthermore, to approximate practical high-speed vehicular scenarios in urban environments, the standardized extended vehicular A (EVA) channel model is adopted in the simulations.

F. Organization and Notation

Organization: Section II presents the system model of the proposed RIS-OTFS-FTN scheme, including the signal model in the DD domain and the corresponding input–output relationship. Section III provides the theoretical performance analysis, covering the AFER, spectral efficiency, and PAPR, etc. An optimal strategy of RIS phase adjustment is designed in Section IV. Section V presents extensive simulation results under the standardized EVA channel model to validate the analytical findings and to provide additional performance insights. Finally, Section VI concludes the paper.

Notation: The superscripts $(\cdot)^T$, $(\cdot)^H$, and $(\cdot)^\dagger$ denote the transpose, Hermitian (conjugate) transpose, and conjugate transpose, respectively, where $(\cdot)^H \equiv (\cdot)^\dagger$. The operator $\text{diag}(\cdot)$ forms a diagonal matrix from its vector argument, and $\text{diag}(\lambda_1, \dots, \lambda_r)$ denotes a diagonal matrix with diagonal entries $\lambda_1, \dots, \lambda_r$. The operator $\text{vec}(\cdot)$ stacks the columns of a matrix into a single column vector. The notation \mathbb{I}_n denotes the $n \times n$ identity matrix, and \mathbb{I}_{MN} denotes the $(MN) \times (MN)$ identity matrix. The set $\mathbb{C}^{m \times n}$ represents the space of $m \times n$ complex-valued matrices, and \mathbb{C} denotes the set of complex numbers. The Euclidean norm is denoted by $\|\cdot\|$, and $|\cdot|$ denotes the absolute value of a scalar. The operator $\text{rank}(\cdot)$ denotes the rank of a matrix, and $\det(\cdot)$ denotes the determinant. The operator $\text{spec}(\cdot)$ denotes the set of eigenvalues of a matrix, representing its spectrum. The notation $\lfloor \cdot \rfloor$ is the floor (integer part) operator. The circular convolution is denoted by \circledast , and \otimes represents the Kronecker product. The notation $\delta(\cdot)$ represents the Dirac delta function. The real part of a complex

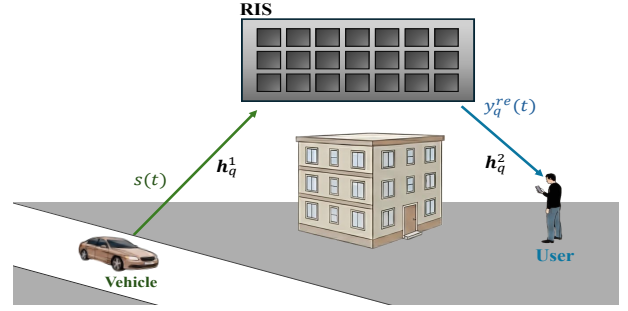


Fig. 1. System model of the RIS-OTFS-FTN schemes.

number x is denoted by $\Re\{x\}$. The expectation operator is denoted by $\mathbb{E}[\cdot]$, and $\Pr(\cdot)$ denotes probability. The notation \mathcal{S} represents the codebook set, with $|\mathcal{S}|$ being its cardinality. The operator $\log_2(\cdot)$ denotes the base-2 logarithm. The notation $z_i \sim \mathcal{CN}(0, \sigma^2)$ indicates that the i -th entry follows a zero-mean circularly symmetric complex Gaussian distribution with variance σ^2 . The exponential function is denoted by both $\exp(\cdot)$ and $e^{(\cdot)}$, which, while distinct in notation, convey the identical mathematical concept. $h(\cdot)$ is differential entropy.

II. SYSTEM MODEL

A. Transmitted Signals

For the proposed scheme, we define M and N as the number of delay and Doppler bins, respectively. Considering the FTN mapper in our scheme, we also define Δf as the subcarrier spacing and FTN-specific symbol interval $T_F = T/M = \alpha T_0$ ($0 < \alpha \leq 1$), where T_F is shorter than that defined under ISI-free Nyquist criterion T_0 , T represents the frame duration, and α is the compression factor in the time domain. Also, let $\mathbf{X}^{\text{DD}} \in \mathbb{C}^{M \times N}$ be the matrix of DD domain symbols in each OTFS frame and $\mathbf{X}^{\text{DD}} = \{x[l, k]\}_{l=0, k=0}^{M-1, N-1}$. Each $x[l, k]$ is modulated by M -ary quadrature amplitude modulation (QAM) with average power $E_x = E[|x[l, k]|^2] = \sigma_x^2$, and placed in the right places after adding cyclic prefix (CP). By using the inverse symplectic fast Fourier transform (ISFFT), \mathbf{X}^{DD} can be transformed into the TF domain as

$$X[m, n] = \frac{1}{\sqrt{MN}} \sum_{l=0}^{M-1} \sum_{k=0}^{N-1} x[l, k] e^{j2\pi(\frac{ml}{M} - \frac{nk}{N})}, \quad (1)$$

where $m = 0, 1, \dots, M-1$ and $n = 0, 1, \dots, N-1$ are m -th and n -th time and frequency bin in the TF grid, respectively. Next, to achieve FTN processing, Heisenberg transform and a root raised-cosine (RRC) pulse shaping filter with a roll-off factor β is employed in $X[m, n]$, which is given as

$$s(t) = \sum_{m=0}^{M-1} \sum_{n=0}^{N-1} X[m, n] g_{tx}(t - n\alpha T_0) e^{j2\pi m \Delta f_0 (t - n\alpha T_0)}, \quad (2)$$

where $g_{tx}(t - n\alpha T_0)$ is the band-limited impulse response shaped by the RRC filter, as the first specific characteristic in our scheme and differing with the rectangular pulses adopted in the conventional schemes.

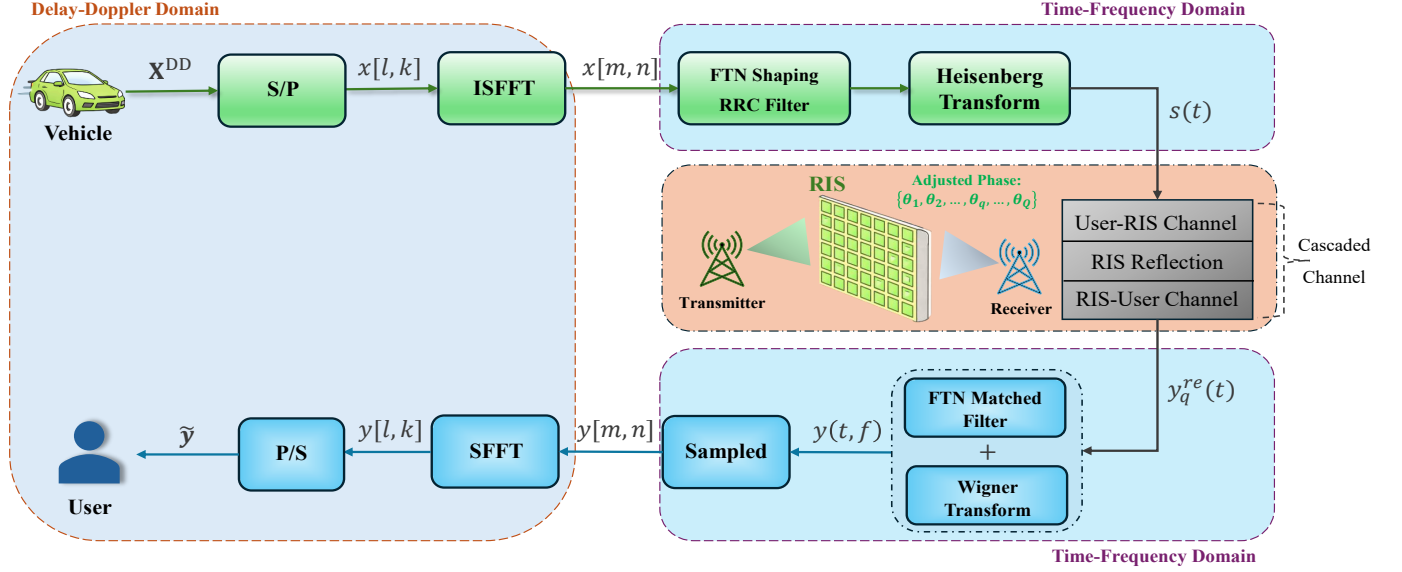


Fig. 2. Signal processing of the RIS-OTFS-FTN scheme.

B. Channel Models

According to Fig. 1, an urban environment with many buildings is considered, where we focus on the V2X communications from the vehicle to the fast-moving user and the direct link from vehicle to user is blocked by barriers. Thus, we consider the time-varying channels from vehicle to the q -th reflection element of RIS and from the q -th reflection element to user, which are respectively given in DD domain as

$$\mathbf{h}_q^1(\tau_q^1, \nu_q^1) = \sum_{p_1=0}^{P_1-1} h_{q,p_1}^1 \delta(\tau_q^1 - \tau_{q,p_1}^1) \delta(\nu_q^1 - \nu_{q,p_1}^1), \quad (3)$$

and

$$\mathbf{h}_q^2(\tau_q^2, \nu_q^2) = \sum_{p_2=0}^{P_2-1} h_{q,p_2}^2 \delta(\tau_q^2 - \tau_{q,p_2}^2) \delta(\nu_q^2 - \nu_{q,p_2}^2), \quad (4)$$

with $\delta(\cdot)$ representing the Dirac's delta function, h_{q,p_1}^1 and h_{q,p_2}^2 , τ_q^1 and τ_q^2 , ν_q^1 and ν_q^2 denoting channel gain, delay, and Doppler of q -th reflection element for p_1 -th and p_2 -th paths, P_1 and P_2 representing number of paths for both links. Moreover, we can further express τ_{q,p_1}^1 and τ_{q,p_2}^2 , ν_{q,p_1}^1 and ν_{q,p_2}^2 as

$$\begin{aligned} \tau_{q,p_1}^1 &= \frac{l_{p_1}}{M\Delta f} \quad \text{and} \quad \nu_{q,p_1}^1 = \frac{r_{p_1} + \kappa_{p_1}}{NT_F}, \\ \tau_{q,p_2}^2 &= \frac{l_{p_2}}{M\Delta f} \quad \text{and} \quad \nu_{q,p_2}^2 = \frac{r_{p_2} + \kappa_{p_2}}{NT_F}, \end{aligned} \quad (5)$$

where l_{p_1} and l_{p_2} represent the delay taps for p_1 and p_2 paths, $r_{p_1} + \kappa_{p_1}$ and $r_{p_2} + \kappa_{p_2}$ are the Doppler shift taps of p_1 and p_2 paths. Note that l_{p_1} , l_{p_2} , r_{p_1} , and r_{p_2} are all integers, but κ_{p_1} and κ_{p_2} are the fractional parts with the range in $(-\frac{1}{2}, \frac{1}{2})$.¹ Based on (3) and (4), by applying inverse Fourier transform,

¹In practical wireless channels, Doppler shifts are continuous values that rarely align exactly with the discrete Doppler bins defined by the system. Therefore, a fractional Doppler component is introduced to accurately model the true Doppler shift and avoid performance degradation caused by quantization errors.

we can obtain channel responses of vehicle-RIS and RIS-user links in time domain as

$$\begin{aligned} \mathbf{h}_q^1(t) &= \int_{-\infty}^{\infty} \mathbf{h}_q^1(\tau_q^1, \nu_q^1) e^{j2\pi\nu_q^1(t-\tau_q^1)} d\nu_q^1 \\ &= \sum_{p_1=0}^{P_1-1} h_{q,p_1}^1 e^{j2\pi\nu_{q,p_1}^1(t-\tau_{q,p_1}^1)} \delta(\tau - \tau_{q,p_1}^1), \end{aligned} \quad (6)$$

and

$$\begin{aligned} \mathbf{h}_q^2(t) &= \int_{-\infty}^{\infty} \mathbf{h}_q^2(\tau_q^2, \nu_q^2) e^{j2\pi\nu_q^2(t-\tau_q^2)} d\nu_q^2 \\ &= \sum_{p_2=0}^{P_2-1} h_{q,p_2}^2 e^{j2\pi\nu_{q,p_2}^2(t-\tau_{q,p_2}^2)} \delta(\tau - \tau_{q,p_2}^2). \end{aligned} \quad (7)$$

C. Received Signals

Firstly, let us focus on the received signals on the RIS. For each reflection element, we define $y_q^{ris}(t)$ as the received signal on the q -th reflection element corresponding to the incident signal $s(t)$ from vehicle. Specifically, $y_q^r(t)$ in time domain can be expressed as

$$y_q^{ris}(t) = \sum_{p_1=0}^{P_1-1} h_{q,p_1}^1 e^{j2\pi\nu_{q,p_1}^1(t-\tau_{q,p_1}^1)} s(t - \tau_{q,p_1}^1). \quad (8)$$

Therefore, after adjusting by the RIS, the reflecting signals to receiver can be expressed as

$$\begin{aligned} y_q^{re}(t) &= \beta_q e^{j\theta_q} y_q^{ris}(t) \\ &= \beta_q e^{j\theta_q} \sum_{p_1=0}^{P_1-1} h_{q,p_1}^1 e^{j2\pi\nu_{q,p_1}^1(t-\tau_{q,p_1}^1)} s(t - \tau_{q,p_1}^1), \end{aligned} \quad (9)$$

where $\beta_q e^{j\theta_q}$ is the reflection coefficient of q -th reflection element with amplitude attenuation $\beta_q \in [0, 1]$ and adjusted phase $\theta_q \in [0, 2\pi]$. Next, we can simply obtain the received

signals from q -th to receiver, which is given as

$$y_q(t) = \sum_{p_1=0}^{P_1-1} \sum_{p_2=0}^{P_2-1} h_{q,p_2}^2 e^{j2\pi\nu_{q,p_2}^2(t-\tau_{q,p_1}^1-\tau_{q,p_2}^2)} \beta_q e^{j\theta_q} h_{q,p_1}^1 e^{j2\pi\nu_{q,p_1}^1(t-\tau_{q,p_1}^1-\tau_{q,p_2}^2)} s(t-\tau_{q,p_1}^1-\tau_{q,p_2}^2) \quad (10)$$

For convenience, we can further rewrite (10) as

$$y_q(t) = \Phi_q \sum_{p_1=0}^{P_1-1} \sum_{p_2=0}^{P_2-1} h_{q,p_1,2}^{\text{eff}} e^{j2\pi\nu_{q,p_1,2}^{\text{eff}}(t-\tau_{q,p_1,2}^{\text{eff}})} s(t-\tau_{q,p_1,2}^{\text{eff}}), \quad (11)$$

where $\Phi_q = \beta_q e^{j\theta_q}$, $h_{q,p_1,2}^{\text{eff}} = h_{q,p_1}^1 h_{q,p_2}^2$, $\nu_{q,p_1,2}^{\text{eff}} = \nu_{q,p_1}^1 + \nu_{q,p_2}^2$, and $\tau_{q,p_1,2}^{\text{eff}} = \tau_{q,p_1}^1 + \tau_{q,p_2}^2$. Eventually, by defining Q as number of total reflection elements, the received signals from RIS with total reflection elements to receiver can be given as

$$y(t) = \sum_{q=1}^Q y_q(t) = \sum_{q=1}^Q \sum_{p_1=0}^{P_1-1} \sum_{p_2=0}^{P_2-1} h_{q,p_1,2}^{\text{eff}} \Phi_q e^{j2\pi\nu_{q,p_1,2}^{\text{eff}}(t-\tau_{q,p_1,2}^{\text{eff}})} s(t-\tau_{q,p_1,2}^{\text{eff}}). \quad (12)$$

Based on FTN processing at receiver, we consider the window function of RRC filter as $g_{rx}(t) = g_{tx}^*(-t)$, which is used to facilitate the conversion of the incoming signal $y(t)$ into TF domain by Wigner transform. Specifically, it can be expressed as

$$y(t, f) = \int g_{rx}^*(t' - t) y(t') e^{-j2\pi f(t' - t)} dt'. \quad (13)$$

Furthermore, via matched filter at frequency $f = m\Delta f_0$ and time $t = n\alpha T_0$, signals in (13) need to be sampled in TF domain, which is given as

$$y[m, n] = y(t, f) |_{t=n\alpha T_0, f=m\Delta f}. \quad (14)$$

Finally, by employing symplectic fast Fourier transform (SFFT), we can obtain received signals in DD domain, which is given as

$$y[l, k] = \frac{1}{\sqrt{MN}} \sum_{m=0}^{M-1} \sum_{n=0}^{N-1} y[m, n] e^{-j2\pi(\frac{ml}{M} - \frac{nk}{N})}. \quad (15)$$

Detail illustration of signal processing in our scheme is shown in Fig. 2.

D. Input-Output Relation in DD Domain

In order to represent the RIS-assisted OTFS system in the discrete DD domain, we firstly quantize the continuous-time delay $\tau_{q,p_1,2}$ and Doppler $\nu_{q,p_1,2}$ values to their corresponding discrete taps. Given an OTFS grid with M delay bins and N Doppler bins, the resolutions are defined as

$$\Delta\tau = \frac{1}{M\Delta f}, \quad \Delta\nu = \frac{1}{NT_F}, \quad (16)$$

where Δf is the subcarrier spacing and T_F is the symbol duration via FTN. Moreover, for a given path with continuous delay and Doppler values $(\tau_{q,p_1,2}, \nu_{q,p_1,2})$, the corresponding discrete delay tap $\varepsilon_{q,p_1,2}$ and Doppler tap $k_{q,p_1,2}$ are given by

$$\varepsilon_{q,p_1,2} = \lfloor \tau_{q,p_1,2} M\Delta f \rfloor, \quad k_{q,p_1,2} = \lfloor \nu_{q,p_1,2} NT_F \rfloor. \quad (17)$$

After this, we continue to formulate the input-output relationship in the discrete DD domain. Considering both the direct vehicle-user channel and the cascaded vehicle-RIS-user channels, the received time-domain signal at a -th element in DD 2D grid can be expressed as Eq. (18) at the top in next page, where $s[a]$ is the time-domain symbol at a -th element in DD 2D grid. Moreover, (18) can be compactly written in vector form as

$$\tilde{\mathbf{y}} = \sum_{q=1}^Q \Phi_q \tilde{\mathbf{H}}_q \tilde{\mathbf{s}}, \quad (19)$$

where $\tilde{\mathbf{s}} \in \mathbb{C}^{NM \times 1}$ and $\tilde{\mathbf{y}} \in \mathbb{C}^{NM \times 1}$ respectively represents the transmitted and the received data vector in time domain with $\tilde{\mathbf{y}} = \{y[a]\}_{a=0}^{MN-1}$ and $\tilde{\mathbf{s}} = \{s[a]\}_{a=0}^{MN-1}$, and $\tilde{\mathbf{H}}_q \in \mathbb{C}^{NM \times NM}$ is the cascaded channel matrix with cascaded coefficient h_q .

Applying OTFS modulation and demodulation, e.g., ISFFT in Eq. (1), Heisenberg transform in Eq. (2), Wigner transform with FTN-included ISI in Eq. (13) and sampling, we can obtain cascaded channel in TF domain as $\mathbf{H}_{\text{TF}}^{\text{eff}}$ with $\{\mathbf{H}_{\text{TF}}^{\text{eff}}\}_{n,m} = \mathbf{H}_q[m, n]$. Given that DD-domain channel gain matrix $\mathbf{H}_{\text{TF},q}$ for the q -th RIS element, in which non-zero entry corresponds to the complex gain, denoted as $h_{q,p_1,2,a}$, which is expressed as Eq. (20) at the top of next page, with $q = 0, 1, \dots, Q$, $n = 0, 1, \dots, NM - 1$, $m = 0, 1, \dots, MN - 1$, $\zeta = n - M \lfloor \frac{n}{M} \rfloor$, $\zeta' = m - M \lfloor \frac{m}{M} \rfloor$, and $g(t) \triangleq g_{\text{tx}}(t) \star g_{\text{rx}}^*(-t)$.

Let $\mathbf{X}^{\text{DD}} \in \mathbb{C}^{M \times N}$ denote the transmitted symbol matrix in the DD domain, whose (m, n) -th entry carries the data symbol mapped onto the DD grid. For notational convenience, we define the vectorized DD-domain symbol block as $\mathbf{x}^{\text{DD}} \triangleq \text{vec}(\mathbf{X}^{\text{DD}}) \in \mathbb{C}^{MN \times 1}$. Next, applying SFFT as Eq. (15), the matrix-form system output in the DD domain becomes [27]:

$$\mathbf{y} = \mathbf{H}^{\text{eff}} \mathbf{x}^{\text{DD}} + \mathbf{z}^{\text{DD}}, \quad (21)$$

where $\mathbf{H}^{\text{eff}} = [\mathbf{H}_1, \mathbf{H}_2, \dots, \mathbf{H}_Q] \Phi$ with $\Phi = \text{diag}(\beta_1 e^{j\theta_1}, \dots, \beta_Q e^{j\theta_Q}) \otimes \mathbb{I}_{NM}$ and $\mathbf{H}_q \in \mathbb{C}^{NM \times NM}$ is the channel coefficient matrices of the cascaded channel², and $\mathbf{z}^{\text{DD}} = (\mathbf{F}_N \otimes \mathbf{F}_M^H) \mathbf{z}_{\text{TF}}$, $\mathbf{z}_{\text{TF}} \in \mathbb{C}^{MN \times 1}$ is the vector of time domain additive colored complex Gaussian noise with covariance $\mathbb{E}[\mathbf{z}_{\text{TF}} \mathbf{z}_{\text{TF}}^H] = \sigma^2 \mathbf{G}$, where \mathbf{G} is the Toeplitz correlation matrix determined by the FTN pulse shaping. Moreover, $\mathbf{F}_N \in \mathbb{C}^{N \times N}$ and $\mathbf{F}_M \in \mathbb{C}^{M \times M}$ denote the normalized Discrete Fourier

²Specifically, each element of the effective channel matrix $\mathbf{H}_q \in \mathbb{C}^{NM \times NM}$ at row u and column v (where $0 \leq u, v \leq NM - 1$) is explicitly given by the discretized ambiguity function as $[\mathbf{H}_q]_{u,v} = \sum_{p=1}^L h_p e^{j\vartheta_p} \mathcal{A}_g(\frac{u-v}{NM} T_f - \tau_p, \frac{u-v}{NM} \Delta f - \nu_p)$, where L is the number of propagation paths, h_p is the path gain, ϑ_p includes the RIS phase shift, (τ_p, ν_p) are the delay and Doppler shifts of the p -th path and $\mathcal{A}_g(\tau, \nu) = \int g_{\text{tx}}(t) g_{\text{rx}}^*(t - \tau) e^{-j2\pi\nu t} dt$ represents the cross-ambiguity function of the transmit and receive pulse shaping filters, which inherently accounts for the inter-symbol interference induced by FTN signaling.

$$y[a] = \sum_{q=1}^Q \sum_{p_1=0}^{P_1-1} \sum_{p_2=0}^{P_2-1} h_{q,p_1,2}^{\text{eff}} \Phi_q e^{j2\pi \frac{k_{q,p_1,2}(a-\varepsilon_{q,p_1,2})}{NM}} g(t - (a + \varepsilon_{q,p_1,2}) T_f) s[[a - \varepsilon_{q,p_1,2}]_{NM}], \quad (18)$$

$$\mathbf{H}_{\text{TF},q}[m, n] = \begin{cases} \sum_{p_1=0}^{P_1-1} \sum_{p_2=0}^{P_2-1} h_{q,p_1,2,a}^{\text{eff}} e^{j2\pi \frac{k_{q,p_1,2}(a-\varepsilon_{q,p_1,2})}{NM}} g(mT_f - (n + \varepsilon_{q,p_1,2})T_f), & a = [n - m]_{NM}, \zeta \geq \zeta \\ \sum_{p_1=0}^{P_1-1} \sum_{p_2=0}^{P_2-1} h_{q,p_1,2,a}^{\text{eff}} e^{j2\pi \frac{k_{q,p_1,2}(a-\varepsilon_{q,p_1,2})}{NM}} g(mT_f - (n + \varepsilon_{q,p_1,2})T_f), & a = [n - m + M]_{NM}, \zeta < \zeta \\ 0, & \text{otherwise} \end{cases} \quad (20)$$

Transform (DFT) matrices. The (k, l) -th entry of \mathbf{F}_N is given by $[\mathbf{F}_N]_{k,l} = \frac{1}{\sqrt{N}} e^{-j\frac{2\pi}{N}(k-1)(l-1)}$, $1 \leq k, l \leq N$, and \mathbf{F}_M is defined similarly with dimension M .

We note that FTN signaling disrupts the standard OTFS block-circulant property, resulting in a block-Toeplitz effective channel \mathbf{H}^{eff} . Although this precludes circular convolution-based equalization, the matrix remains sparse and banded due to localized pulse shaping, which is efficiently handled by the adopted LMMSE detector.

E. Linear Minimum Mean Square Error Detector

In this work, taking into account the trade-off between complexity and error performance, the Linear Minimum Mean Square Error (LMMSE) detector is employed for the proposed scheme, instead of the maximum likelihood (ML) or message-passing (MP) detectors. Although the vehicle-RIS channel matrix \mathbf{H}_1 and RIS-user channel matrix \mathbf{H}_2 are individually sparse, the cascaded effective channel matrix $\mathbf{H}^{\text{eff}} = \mathbf{H}_2 \Phi \mathbf{H}_1$ loses its sparsity after matrix multiplication [23]. This leads to increased complexity and degraded error performance for the MP detector, as the density of the factor graph increases significantly. Second, the optimal ML detector requires an exhaustive search over all potential symbol combinations, calculating Euclidean distances for the entire NM -dimensional vector space. This results in prohibitively high computational complexity that scales exponentially with the grid size, rendering it impractical for high-mobility OTFS systems. Consequently, we adopt the LMMSE detector [32], which minimizes the mean square error under the constraint of a linear filter. The LMMSE detection based on the structured colored noise is given by:

$$\hat{\mathbf{x}}^{\text{DD}} = \left(\mathbf{H}_{\text{eff}}^\dagger \mathbf{H}_{\text{eff}} + \sigma^2 \mathbf{G} \right)^{-1} \mathbf{H}_{\text{eff}}^\dagger \mathbf{y}, \quad (22)$$

where $\hat{\mathbf{x}}^{\text{DD}} \in \mathbb{C}^{NM \times 1}$ denotes the estimated signal vector. Here, $\mathbf{H}_{\text{eff}}^\dagger$ is the conjugate transpose of the effective channel matrix \mathbf{H}_{eff} .

III. PERFORMANCE ANALYSIS

In this section, based on the received signals in DD domain for our schemes (21), the analytical performance of AFER and

spectral efficiency is provided with closed-form expressions. Moreover, the CCDF of the PAPR and IBO are also given respectively in sub-section C and D of this section. More interesting findings and insights are also given in this section.

A. AFER

While the ML detector is challenging to implement in both practical systems and simulations, its theoretical performance can still be characterized by deriving the upper bound of the AFER, which allows us to gain valuable insights into its fundamental behavior.³ We define E_f as the energy per frame with $E_f = MNE_x$. Let $\mathbf{x}^{\text{DD}} = \text{vec}(\mathbf{X}^{\text{DD}}) \in \mathbb{C}^{NM \times 1}$ denote the vectorized transmitted symbol block. According to the system model, \mathbf{x}^{DD} is drawn from a finite codebook \mathcal{S} with size $|\mathcal{S}|$, where $\mathcal{S} = \{\mathbf{x}_1^{\text{DD}}, \mathbf{x}_2^{\text{DD}}, \dots, \mathbf{x}_{|\mathcal{S}|}^{\text{DD}}\}$.

Given that the FTN-induced noise \mathbf{z} follows a colored Gaussian distribution with covariance Σ_z , the optimal ML detector minimizes the Mahalanobis distance rather than the Euclidean distance. Thus, the detection rule is expressed as

$$\begin{aligned} \hat{\mathbf{x}}^{\text{DD}} &= \arg \min_{\mathbf{x}^{\text{DD}} \in \mathcal{S}} (\mathbf{y} - \mathbf{H}^{\text{eff}} \mathbf{x})^H \Sigma_z^{-1} (\mathbf{y} - \mathbf{H}^{\text{eff}} \mathbf{x}) \\ &= \arg \min_{\mathbf{x}^{\text{DD}} \in \mathcal{S}} \|\mathbf{y} - \mathbf{H}^{\text{eff}} \mathbf{x}^{\text{DD}}\|_{\Sigma_z^{-1}}^2, \end{aligned} \quad (23)$$

where $\|\mathbf{u}\|_{\Sigma_z^{-1}}^2 \triangleq \mathbf{u}^\dagger \Sigma_z^{-1} \mathbf{u}$ denotes the squared Mahalanobis norm. Based on the classical union bound technique, the AFER is upper bounded as

$$P_f \leq \frac{1}{|\mathcal{S}|} \sum_i \sum_{j \neq i} P(\mathbf{x}_i^{\text{DD}} \rightarrow \mathbf{x}_j^{\text{DD}}), \quad (24)$$

where $P(\mathbf{x}_i^{\text{DD}} \rightarrow \mathbf{x}_j^{\text{DD}})$ is the pairwise error probability (PEP). Substituting $\mathbf{y} = \mathbf{H}^{\text{eff}} \mathbf{x}_i^{\text{DD}} + \mathbf{z}$ into (23), the PEP event corresponds to the inequality:

$$\|\mathbf{H}^{\text{eff}} (\mathbf{x}_i^{\text{DD}} - \mathbf{x}_j^{\text{DD}}) + \mathbf{z}\|_{\Sigma_z^{-1}}^2 \leq \|\mathbf{z}\|_{\Sigma_z^{-1}}^2. \quad (25)$$

³Our analysis uses the optimal ML detector as a benchmark. The derived ML upper bound rigorously captures the system's inherent diversity order and coding gain, defining its performance potential. The LMMSE simulations, meanwhile, demonstrate the practical performance achievable under specific receiver constraints.

Expanding the Mahalanobis norm and canceling the common term $\mathbf{z}^\dagger \Sigma_z^{-1} \mathbf{z}$ yields

$$2\Re \{ \mathbf{z}^\dagger \Sigma_z^{-1} \mathbf{H}^{\text{eff}} \Delta_{ij} \} \leq -\Delta_{ij}^\dagger (\mathbf{H}^{\text{eff}})^\dagger \Sigma_z^{-1} \mathbf{H}^{\text{eff}} \Delta_{ij}, \quad (26)$$

where $\Delta_{ij} = \mathbf{x}_i^{\text{DD}} - \mathbf{x}_j^{\text{DD}}$ is the error difference vector. The term on the left-hand side, denoted as $w = \mathbf{z}^\dagger \Sigma_z^{-1} \mathbf{H}^{\text{eff}} \Delta_{ij}$, is a scalar Gaussian random variable with zero mean. Its variance is explicitly derived as

$$\begin{aligned} \sigma_w^2 &= \mathbb{E}[w w^\dagger] \\ &= \Delta_{ij}^\dagger (\mathbf{H}^{\text{eff}})^\dagger \Sigma_z^{-1} \underbrace{\mathbb{E}[\mathbf{z} \mathbf{z}^\dagger]}_{\Sigma_z} \Sigma_z^{-1} \mathbf{H}^{\text{eff}} \Delta_{ij} \\ &= \Delta_{ij}^\dagger (\mathbf{H}^{\text{eff}})^\dagger \Sigma_z^{-1} \mathbf{H}^{\text{eff}} \Delta_{ij}. \end{aligned} \quad (27)$$

Using the Q-function and Chernoff bound [33], [34], the PEP is finally upper-bounded by

$$\begin{aligned} P(\mathbf{x}_i^{\text{DD}} \rightarrow \mathbf{x}_j^{\text{DD}}) &= Q \left(\sqrt{\frac{\Delta_{ij}^\dagger (\mathbf{H}^{\text{eff}})^\dagger \Sigma_z^{-1} \mathbf{H}^{\text{eff}} \Delta_{ij}}{2}} \right) \\ &\leq \exp \left(-\frac{\Delta_{ij}^\dagger (\mathbf{H}^{\text{eff}})^\dagger \Sigma_z^{-1} \mathbf{H}^{\text{eff}} \Delta_{ij}}{4} \right). \end{aligned} \quad (28)$$

In the other hand, let us define the frame difference vector as $\Delta_{ij} = \mathbf{X}_i^{\text{DD}} - \mathbf{X}_j^{\text{DD}}$. Then the exponent term in (28) can be rewritten as a quadratic form

$$\Delta_{ij}^\dagger \mathbf{H}_{\text{eff}}^\dagger \Sigma_z^{-1} \mathbf{H}_{\text{eff}} \Delta_{ij} = \text{vec}(\mathbf{H}_{\text{eff}})^\dagger (\Delta_{ij} \Delta_{ij}^\dagger \otimes \Sigma_z^{-1}) \text{vec}(\mathbf{H}_{\text{eff}}). \quad (29)$$

With assumption that \mathbf{H}^{eff} is composed of i.i.d. Rayleigh fading coefficients, each \tilde{h}_n follows an independent Gaussian distribution with zero mean and variance σ_h^2 , i.e., $\tilde{h}_n \sim \mathcal{CN}(0, \sigma_h^2)$. We can use the well-known moment-generating function (MGF) of complex Gaussian quadratic forms. For any Hermitian positive semidefinite matrix \mathbf{A} , we have

$$\mathbb{E} \left[e^{-\text{vec}(\mathbf{H}_{\text{eff}})^\dagger \mathbf{A} \text{vec}(\mathbf{H}_{\text{eff}})} \right] = \det(\mathbf{I} + \sigma_h^2 \mathbf{A})^{-1}. \quad (30)$$

Applying this result with $\mathbf{A} = \frac{1}{4} (\Delta_{ij} \Delta_{ij}^\dagger \otimes \Sigma_z^{-1})$, the PEP expression can be further expressed as

$$P(\mathbf{X}_i^{\text{DD}} \rightarrow \mathbf{X}_j^{\text{DD}}) \leq \det \left(\mathbf{I} + \frac{\sigma_h^2}{4} \Delta_{ij} \Delta_{ij}^\dagger \otimes \Sigma_z^{-1} \right)^{-1}. \quad (31)$$

To obtain a more interpretable expression, let $\{\lambda_n^{(ij)}\}_{n=1}^{r_{ij}}$ denote the non-zero eigenvalues of $\Delta_{ij} \Delta_{ij}^\dagger$, and let $\{\nu_m\}_{m=1}^{MN}$ denote the eigenvalues of Σ_z^{-1} . Using the Kronecker product property in $\text{spec}(A \otimes B) = \{\lambda_n(A) \nu_m(B)\}$, (31) can be equivalently expressed as

$$P(\mathbf{X}_i^{\text{DD}} \rightarrow \mathbf{X}_j^{\text{DD}}) \leq \prod_{n=1}^{r_{ij}} \prod_{m=1}^{MN} \left(1 + \frac{\sigma_h^2}{4} \lambda_n^{(ij)} \nu_m \right)^{-1}. \quad (32)$$

Finally, substituting (32) into the union bound (24), we obtain the AFER upper bound as

$$P_f \leq \frac{1}{|\mathcal{S}|} \sum_{i=1}^{|\mathcal{S}|} \sum_{\substack{j=1 \\ j \neq i}}^{|\mathcal{S}|} \prod_{n=1}^{r_{ij}} \prod_{m=1}^{MN} \left(1 + \frac{\sigma_h^2}{4} \lambda_n^{(ij)} \nu_m \right)^{-1}. \quad (33)$$

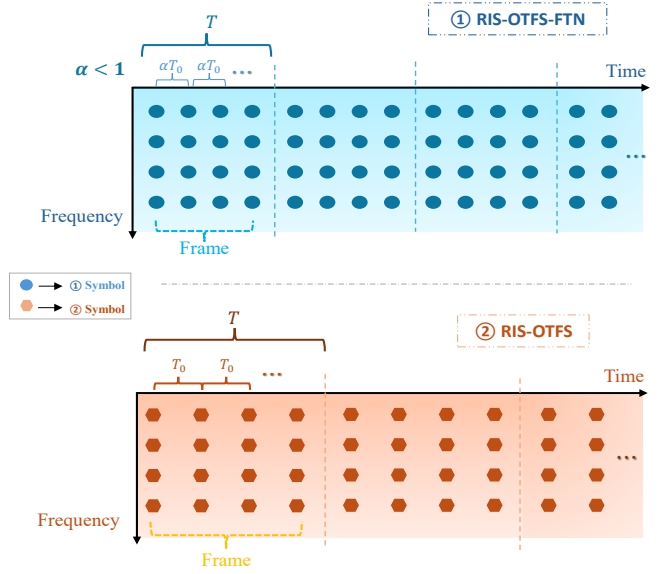


Fig. 3. Comparison between RIS-OTFS schemes with and without FTN in TF domain.

Remark 1: A higher E_f enhances signal strength, reducing the error probability, and this effect is indirectly reflected through the channel gain and symbol energy distribution. Besides, due to $E_f = MNE_x$, when M and N increase, E_f grows linearly, and $\text{SNR} = \frac{E_f}{\sigma^2} \propto MN$ increases. Note that Σ_z and \mathbf{G} are positive-definite matrices. In the formula, the number of terms in $\prod_{m=1}^{MN}$ rises from MN to $M'N'$ with more ν_m terms involved, leading to lower AFER.

Remark 2: From the eigenvalue decomposition of the PEP upper bound in (28), let $r_{ij} \triangleq \text{rank}(\Delta_{ij} \Delta_{ij}^\dagger) = \text{rank}(\Delta_{ij})$ denote the number of non-zero eigenvalues of the error difference matrix $\Delta_{ij} \Delta_{ij}^\dagger$. Given that the FTN-induced noise covariance $\Sigma_z = \sigma^2 \mathbf{G}(\alpha)$ is positive definite, its inverse eigenvalues scale as $\nu_m(\alpha) = \mu_m(\alpha) / \sigma^2$, where $\{\mu_m(\alpha)\}$ are the eigenvalues of $\mathbf{G}^{-1}(\alpha)$ which are independent of the noise power σ^2 . In the high-SNR regime, each term in the product expansion behaves as $(1 + c \lambda_n^{(ij)} \nu_m(\alpha))^{-1} \doteq \text{SNR}^{-1}$. This yields the asymptotic decay rate of the error probability as

$$P(\mathbf{x}_i^{\text{DD}} \rightarrow \mathbf{x}_j^{\text{DD}}) \doteq \text{SNR}^{-MN \cdot r_{ij}}. \quad (34)$$

Thus, asymptotic diversity order is given by $d = MN \cdot \min_{i \neq j} r_{ij}$. Crucially, the FTN acceleration factor α modifies the eigen-spectrum $\{\mu_m(\alpha)\}$ of the correlation matrix $\mathbf{G}(\alpha)$, thereby affecting coding gain. However, it does not alter the diversity exponent (slope) as long as $\mathbf{G}(\alpha)$ remains full rank.

B. Spectral Efficiency

In order to obtain the final expression of spectral efficiency, let us firstly derive the expression of mutual information for per frame of our scheme. According to (21), the mutual information between \mathbf{X}_{DD} and \mathbf{y} is defined as

$$I(\mathbf{X}_{\text{DD}}; \mathbf{y}) = h(\mathbf{y}) - h(\mathbf{y} | \mathbf{X}_{\text{DD}}), \quad (35)$$

where $h(\cdot)$ denotes the differential entropy. Here, for clear comparisons and presentation, we assume that the input

symbols \mathbf{X}_{DD} are zero-mean circularly symmetric complex Gaussian with covariance matrix Σ_X and the noise vector $\mathbf{z} \sim \mathcal{CN}(0, \Sigma_z)$ is independent of \mathbf{X}_{DD} . Given \mathbf{X}_{DD} , the conditional distribution is $\mathbf{y} | \mathbf{X}_{\text{DD}} \sim \mathcal{CN}(\mathbf{H}^{\text{eff}} \mathbf{X}_{\text{DD}}, \Sigma_z)$, so that we have conditional entropy:

$$\begin{aligned} h(\mathbf{y} | \mathbf{X}^{\text{DD}}) &= h(\mathbf{z}_{\text{DD}}) \\ &= \log_2 \left((\pi e)^{MN} \det(\Sigma_z) \right) \\ &= NM \log_2(\pi e) + \log_2 \left(\det(\Sigma_z) \right), \end{aligned} \quad (36)$$

where e denotes Euler's number, as the base of natural logarithms with approximate value in 2.7183.

Unconditionally, \mathbf{y} is Gaussian with covariance matrix $\mathbf{H}_{\text{eff}} \Sigma_X \mathbf{H}_{\text{eff}}^H + \Sigma_z$. Thus, we can obtain the marginal entropy $h(\mathbf{y})$ as

$$\begin{aligned} h(\mathbf{y}) &= \log_2 \left((\pi e)^{MN} \det(\mathbf{H}^{\text{eff}} \Sigma_X \mathbf{H}_{\text{eff}}^{\dagger} + \Sigma_z) \right) \\ &= \log_2 \det(\mathbf{H}^{\text{eff}} \Sigma_X \mathbf{H}_{\text{eff}}^{\dagger} + \Sigma_z) + NM \log_2(\pi e). \end{aligned} \quad (37)$$

Next, by subtracting the conditional entropy (36) from the marginal entropy (37) yields the final expression of mutual information $I(\mathbf{X}^{\text{DD}}; \mathbf{y})$ as

$$\begin{aligned} I(\mathbf{X}^{\text{DD}}; \mathbf{y}) &= \log_2 \det(\mathbf{H}^{\text{eff}} \Sigma_X \mathbf{H}_{\text{eff}}^{\dagger}) - \log_2 \left(\det(\Sigma_z) \right) \\ &= \log_2 \det \left(\mathbf{I}_{MN} + \Sigma_{z_{\text{DD}}}^{-1} \mathbf{H}_{\text{eff}} \Sigma_X \mathbf{H}_{\text{eff}}^{\dagger} \right) \\ &= \log_2 \det \left(\mathbf{I}_{MN} + \frac{1}{\sigma^2} \mathbf{G}^{-1} \mathbf{H}^{\text{eff}} \Sigma_X \mathbf{H}_{\text{eff}}^{\dagger} \right). \end{aligned} \quad (38)$$

To simplify, perform eigenvalue decomposition (EVD) on $\mathbf{G} = \mathbf{V} \mathbf{\Lambda} \mathbf{V}^H$, where $\mathbf{V} = \text{diag} \{ \lambda_0^1, \lambda_1^1, \dots, \lambda_{MN-1}^1 \}$ with i -th λ_i^1 non-zero eigenvalues of \mathbf{G} . Then, given that $\mathbf{B} = \mathbf{\Lambda}^{-1/2} \mathbf{V}^H \mathbf{H}^{\text{eff}}$, Eq. (38) can be further rewritten as $I(\mathbf{X}_{\text{DD}}; \mathbf{y}) = \log_2 \det \left(\mathbf{I}_{MN} + \frac{E_x}{\sigma^2} \mathbf{B}^H \mathbf{B} \right)$. Let $\mathbf{B}^H \mathbf{B} = \mathbf{U} \mathbf{\Xi} \mathbf{U}^H$ with $\mathbf{\Xi} = \text{diag} \{ \xi_0, \xi_1, \dots, \xi_{MN-1} \}$ and ξ_i being i -th non-zeros eigenvalue of $\mathbf{B}^H \mathbf{B}$. Eq. (38) can be simplified as

$$I(\mathbf{X}_{\text{DD}}; \mathbf{y}) = \sum_{n=0}^{MN-1} \log_2 \left(1 + \frac{E_x \xi_n}{\sigma^2} \right). \quad (39)$$

Eventually, by assuming the energy of each frame is evenly distributed to each symbol, we have a covariance matrix for per frame as $E_x = \frac{E_f}{MN}$, the achievable spectral efficiency of the RIS-OTFS-FTN scheme is defined as the total mutual information per frame normalized by the frame duration as

$$\eta = \frac{1}{M \Delta f N \alpha T_0} \sum_{n=0}^{MN-1} \log_2 \left(1 + \frac{E_f \xi_n}{MN \sigma^2} \right). \quad (40)$$

Remark 3: According to (40), we can easily find that spectral efficiency of our scheme increases with decrease of α , which is inverse in the scheme without FTN due to the absence of α . This also can be learned in Fig. 3, where we can clearly investigate that the RIS-OTFS-FTN scheme can transmit more symbols with [them](#) same time duration to the scheme without FTN, thus enhancing the spectral efficiency. Moreover, it is investigated that the spectral efficiency of our scheme gets

much better in a range of high SNR, while $E_x \gg \sigma^2$. More results and insights are provided in Sec. V.

C. PAPR and CCDF

The PAPR is a critical metric for evaluating the efficiency of power amplifiers in communication systems, particularly in the proposed RIS-OTFS-FTN scheme, where FTN signaling introduces unique signal dynamics [35]. Attention should be paid to the time-domain transmitted signal $s(t)$, as the PAPR is a power metric computed based on the actual transmission waveform. The CCDF provides an intuitive measure of the likelihood of encountering large peaks in the transmit waveform, which is critical for evaluating power amplifier back-off requirements. Also, it quantifies the probability that the PAPR exceeds a specified threshold, offering insights into the statistical characteristics of the signal [35]. In this subsection, we derive the analytical framework for computing the CCDF of the PAPR for the proposed scheme, accounting for the effects of FTN compression and RRC pulse shaping.

Based on Eq. (1), the expression of PAPR is defined as

$$\text{PAPR} = \frac{\max |s(t)|^2}{\mathbb{E}[|s(t)|^2]}, \quad (41)$$

where $\mathbb{E}[|s(t)|^2]$ represents the average power of the signal. For a given threshold γ_0 , the PAPR can be obtained as

$$\begin{aligned} \text{CCDF}(\gamma_0) &= \Pr(\text{PAPR} > \gamma_0) \\ &= 1 - \Pr \left(\max_{t \in [0, T]} \frac{|s(t)|^2}{\mathbb{E}[|s(t)|^2]} \leq \gamma_0 \right). \end{aligned} \quad (42)$$

To obtain the CCDF curve, a large number of frames are generated using Monte Carlo simulations. For each frame, the PAPR is calculated, and the empirical distribution is estimated by counting the proportion of frames whose PAPR exceeds a given threshold γ_0 .

D. IBO

The IBO is a key parameter for assessing the linearity margin of PA and it directly relates to the PAPR of the transmit waveform. In this subsection we distinguish two useful IBO definitions used in our analysis: (i) the *minimum required IBO* that guarantees no clipping of waveform peaks, and (ii) the *available IBO* that results from a given PA saturation level and the transmitter average power. Based on Eq. (41), the required IBO for linear operation is mainly determined by the PAPR of the transmitted signal plus a design margin to avoid nonlinear distortion, expressed as

$$\text{IBO}_{\text{req}} = \text{PAPR} + \gamma_{\text{margin}}, \quad (43)$$

where γ_{margin} typically ranges from 1 to 3 dB to accommodate implementation imperfections.

Meanwhile, the available IBO, which is related to the transmitter hardware capabilities, depends on the difference between the PA saturation power P_{sat} and the average transmit power P_{avg} as

$$\text{IBO}_{\text{avail}} = P_{\text{sat}} - P_{\text{avg}}. \quad (44)$$

To maintain linear amplification and avoid signal distortion, the system must satisfy

$$\text{IBO}_{\text{avail}} \geq \text{IBO}_{\text{req}}. \quad (45)$$

By introducing the RIS, the effective channel gain is enhanced, enabling a reduction in the required transmit power P_{avg} for a given quality-of-service target. This reduction leads to an increase in the available IBO without changing the hardware saturation power P_{sat} , i.e.,

$$\text{IBO}_{\text{avail}}^{\text{RIS}} = P_{\text{sat}} - P_{\text{avg}}^{\text{RIS}} > \text{IBO}_{\text{avail}}^{\text{no RIS}} = P_{\text{sat}} - P_{\text{avg}}^{\text{no RIS}}, \quad (46)$$

where $P_{\text{avg}}^{\text{RIS}}$ and $P_{\text{avg}}^{\text{no RIS}}$ represent the average transmit power with and without the RIS respectively, with $P_{\text{avg}}^{\text{no RIS}} = P_{\text{avg}}^{\text{RIS}} + G_{\text{RIS}}$ and G_{RIS} being the equivalent RIS gain. Therefore, the RIS-assisted system achieves the same linearity requirement in PA with a lower transmission power, reducing power consumption and improving the power amplifier's operating efficiency. This characteristic highlights the advantage of RIS in energy-constrained scenarios, providing a more favorable trade-off between linearity and power efficiency.

In summary, the incorporation of RIS allows for a smaller required IBO in practice or equivalently an increased available IBO for the same transmit power, thereby enhancing system performance and energy efficiency.

E. Complexity Analysis and Scalability

The introduction of FTN induces colored noise and intentional ISI, creating a coupled effective channel structure. However, since the pulse shaping is localized, the FTN processing involves banded convolution scaling linearly as $\mathcal{O}(MNW)$, where W is the effective pulse span. For the RIS configuration, the proposed phase alignment, e.g., Algorithm 1 in Sec. IV, incurs a low complexity of $\mathcal{O}(PQ)$. Crucially, this overhead is amortized over the channel coherence time, as RIS phases are not updated on a per-symbol basis. Regarding detection, while the adopted LMMSE detector theoretically entails $\mathcal{O}((MN)^3)$ complexity via direct inversion, the effective channel matrix retains a banded-block-Toeplitz structure. For practical scalability, this structure can be exploited by advanced banded solvers to reduce the complexity to approximately $\mathcal{O}(N_{\text{sys}}W^2)$, where $N_{\text{sys}} \approx MN$ denotes the dimension of the underlying linear system, i.e., the number of DD symbols per OTFS frame. This ensures that the proposed scheme remains tractable for moderate grid sizes while offering significant spectral efficiency gains.

IV. RIS DESIGN

A. Adjusted Phase Algorithm

In our work, the goal of RIS phase optimization is to adjust the phase shifts of each RIS reflecting element to maximize the effective channel gain at the receiver. A key characteristic of an RIS system is its capability to dynamically reconfigure reflection coefficients in accordance with channel conditions. In OTFS modulation, the channel is represented in the DD domain, where variations occur at a slower rate compared

Algorithm 1 RIS Phase Optimization for RIS-OTFS-FTN with Cascaded Delay-Doppler Channel

- 1: **Input:** Cascaded DD channel responses $\tilde{\mathbf{H}}_q$ for $q = 1, \dots, Q$
- 2: **Initialize:** Phase shifts $\theta_q \in [0, 2\pi)$ and fixed amplitudes $\beta_q = 1$
- 3: Compute the combined unoptimized effective channel by using (47)
- 4: Identify set of non-zero entries $\{h_{\text{tot}}(k_p, l_p)\}_{p=1}^P$ in $\tilde{\mathbf{H}}$
- 5: **for** $p = 1$ to P **do**
- 6: Evaluate power metric by using (48)
- 7: **end for**
- 8: Select strongest path by $p^* = \arg \max_p \text{Power}[p]$
- 9: Let $(k^*, l^*) = (k_{p^*}, l_{p^*})$
- 10: **for** $q = 1$ to Q **do**
- 11: Compute optimal phase shift by using (49)
- 12: Update phase factor: $\phi_q^{\text{opt}} = e^{j\theta_q^{\text{opt}}}$
- 13: **end for**
- 14: Compute optimized channel by $\mathbf{H}_{\text{opt}} = \sum_{q=1}^Q \beta_q \phi_q^{\text{opt}} \cdot \tilde{\mathbf{H}}_q$
- 15: **Output:** Optimized effective channel \mathbf{H}_{opt}

to the time-frequency domain representation. Consequently, the phase adjustment frequency in the RIS can be reduced. Here, we consider the discrete phase adjustment, of which the optimization procedure is described below.

According to (19), we have the cascaded DD channel response of the q -th RIS element be denoted by $\tilde{\mathbf{H}}_q$. Thus, the combined effective channel with phase optimization is expressed as

$$\tilde{\mathbf{H}}_q = \sum_{q=1}^Q \beta_q e^{j\theta_q^v} \tilde{\mathbf{H}}_q, \quad (47)$$

where amplitude attenuation $\beta_q = 1$ is defined in this section for better analysis, $\{\theta_q^v\}_{q=1, v=1}^{Q, V}$ denote a set of discrete adjusted phases with $q \in \{1, 2, \dots, Q\}$ and $v \in \{1, 2, \dots, V\}$, each $\theta_q^v \in [0, 2\pi)$, and the adjusted-phase set is $\{\theta_q^1, \theta_q^2, \dots, \theta_q^V\}$ for each q ,

Let $\{h_{\text{tot}}(k_p, l_p)\}_{p=1}^P$ denote the non-zero entries in $\tilde{\mathbf{H}}_q$ corresponding to P cascaded propagation paths. Among them, the strongest path is selected by maximizing the following metric given as follows:

$$p^* = \arg \max_{p \in \{1, \dots, P\}} \left| h_{\text{tot}}(k_p, l_p) + \sum_{i=1}^L h^{(i)}(k_p, l_p) \right|^2. \quad (48)$$

To align the phase of each RIS element constructively on the selected tap (k^*, l^*) of the strongest path, the optimal phase shift is computed as

$$\theta_i^{\text{opt}} = \arg(h_{\text{tot}}(k^*, l^*)) - \arg(h^{(q)}(k^*, l^*)), \quad (49)$$

with $\arg(\cdot)$ representing the argument of a complex number, and the corresponding optimized phase factor given by $\phi_i^{\text{opt}} = e^{j\theta_i^{\text{opt}}}$. Therefore, after resulting optimized effective channel as $\mathbf{H}_{\text{opt}} = \sum_{i=1}^L \phi_i^{\text{opt}} \cdot \mathbf{h}^{(i)}$, we can respectively obtain the

received signals in time and DD domain as

$$y_{\text{opt}}(t) = \sum_{q=1}^Q \sum_{p_1=0}^{P_1-1} \sum_{p_2=0}^{P_2-1} h_{q,p_1,2}^{\text{eff}} \beta_q e^{j(\theta_1 - \theta_i^{\text{opt}})} s \left(t - \tau_{q,p_1,2}^{\text{eff}} \right),$$

$$y[a] = \sum_{q=1}^Q \sum_{p_1=0}^{P_1-1} \sum_{p_2=0}^{P_2-1} h_{q,p_1,2}^{\text{eff}} \beta_q e^{j(\theta_2 - \theta_i^{\text{opt}})} s \left[[a - \varepsilon_{q,p_1,2}]_{NM} \right] \quad (50)$$

with $\theta_1 = 2\pi\nu_{q,p_1,2}^{\text{eff}}(t - \tau_{q,p_1,2}^{\text{eff}})$ and $\theta_2 = 2\pi \frac{k_{q,p_1,2}(a - \varepsilon_{q,p_1,2})}{NM}$. Detail steps for optimization can be found in Algorithm 1.

Remark 4: According to (40), the spectral efficiency is expected to improve by employing the RIS phase optimization strategy. This is because optimizing the RIS phase shifts enhances the effective channel gain by aligning the reflected signals constructively at the receiver. Thus, the matrix product $\mathbf{H}_{\text{eff}} \mathbf{H}_{\text{eff}}^H$ contains stronger eigenvalues, leading to a larger determinant inside the logarithm. Although random phase adjustment may also increase compared to the case without RIS, which is because random phase configurations can still introduce diversity and enable some constructive interference at the receiver by chance, the effective channel gain \mathbf{H}_{eff} is generally weaker than in the case of optimal phase alignment since the phase shifts are not aligned to maximize the received signal power. Consequently, the performance gain from random phase modulation is typically limited and less consistent. More corresponding results and insights are given in Sec. V.

Remark 5: Identifying the strongest path from $P = P_1 + P_2$ dominant multipath components require $\mathcal{O}(P)$ operations. Subsequently, calculating the optimal phase shifts for Q reflection elements involve $\mathcal{O}(Q)$ complex additions and phase extractions. Therefore, the total computational complexity is in the order of $\mathcal{O}(P + Q)$. Compared to the signal detection complexity, e.g., $\mathcal{O}((NM)^3)$ for LMMSE, the overhead introduced by the RIS phase design can be negligible.

B. Robustness to Channel Estimation Errors

In practical high-mobility scenarios with RIS applications, obtaining perfect channel state information (CSI) is challenging. To evaluate the robustness of the proposed RIS phase alignment strategy, we model the impact of imperfect CSI. For better presentation, we assume the transmitter-to-RIS link, being stationary, is accurately estimated. However, the RIS-to-User link suffers from estimation errors due to user mobility and difficulty of estimating reflecting link. The estimated channel impulse response with imperfect CSI for the RIS-to-User link is modeled as

$$\hat{h}_q^2 = h_q^2 + \mathbf{e}_q, \quad (51)$$

where h_q^2 denotes the vector of path gains $[h_{q,0}^2, \dots, h_{q,P_2-1}^2]^T$ corresponding to the time-domain response in (7), and $\mathbf{e}_q \sim \mathcal{CN}(\mathbf{0}, \delta_{e^2}^2 \mathbf{I})$ represents the channel estimation error vector.

C. Impact of Finite Resolution Phase Quantization

Practical RIS implementations are constrained by hardware limitations, typically supporting only a finite set of

TABLE I
DELAY-POWER PROFILE OF THE EVA CHANNEL MODEL

Path Index	Delay (ns)	Power (dB)	Linear Power
1	0	0.0	0.1964
2	30	-1.5	0.1389
3	150	-1.4	0.1433
4	310	-3.6	0.0870
5	370	-0.6	0.1709
6	710	-9.1	0.0246
7	1090	-7.0	0.0391
8	1730	-12.0	0.0124
9	2510	-16.9	0.0045

discrete phase levels. To evaluate the impact of this practical constraint, we consider a B -bit quantization scheme. The set of feasible discrete phase shifts is defined as $\mathcal{F}_B = \{0, \frac{2\pi}{2^B}, \dots, \frac{2\pi(2^B-1)}{2^B}\}$. Consequently, the continuous optimal phase θ_q^{opt} obtained from Algorithm 1 is quantized to the nearest discrete level $\hat{\theta}_q \in \mathcal{F}_B$. The resulting quantized phase shift matrix, denoted as $\hat{\Phi} = \text{diag}(\beta_1 e^{j\hat{\theta}_1}, \dots, \beta_Q e^{j\hat{\theta}_Q}) \otimes \mathbf{I}_{NM}$, is then applied to the effective channel construction. This quantization introduces a phase mismatch that degrades the passive beamforming gain. The trade-off between the quantization resolution B , e.g., 1, 2, and 3-bit, and the system error performance is numerically investigated in Section V.

V. SIMULATION RESULTS

In this section, theoretical and simulation results of the RIS-OTFS-FTN scheme, e.g., PAPR, CCDF, IBO, FER, BER, and spectral efficiency are provided. Here, to approach the channel environment in suburban or urban high-speed scenarios, a standard EVA wireless channel model is employed in this section⁴. The detail values of simulation parameter in EVA model are given in Table I. For a clear presentation and comparison in this section, several other parameters are also fixed, including size of QAM $M_{QAM} = 2$, carrier frequency $f_c = 4$ GHz, subcarrier spacing $\Delta f = 15$ KHz, unit transmitted energy of each symbol $E_x = 1$, maximum speed for user $v_{max} = 120$ km/h, and SNR as $\frac{E_x}{\sigma^2}$. Two parameters of RRC filter are firstly given, e.g., RRC roll-off factor $\beta_{RRC} = 0.25$ and symbol period span $s_{RRC} = 8$. Moreover, Monte Carlo simulations are conducted with each experiment performed over 3×10^3 independent channel realizations, while considering the large complexity in calculation and running simulation. In consideration of the practical implementation of an RIS, discrete phase shifts with 3 bits allocated to each are adopted for simulation purposes, and the set of feasible values is expressed as $\theta_q^v \in \{0, \frac{2\pi}{8}, \frac{4\pi}{8}, \frac{6\pi}{8}, \pi, \frac{10\pi}{8}, \frac{12\pi}{8}, \frac{14\pi}{8}\}$. The results are presented under the assumption that there

⁴EVA channel model is a representative wireless fading model widely employed for simulating high-mobility environments, such as those encountered in LTE, 5G, and performance evaluations of advanced schemes like the RIS-OTFS-FTN system. As an extended version of the Vehicular A (VA) model recommended by the 3GPP and ITU standards [36], the EVA model features a longer delay spread and more complex multi-path characteristics. These enhancements allow it to more accurately capture the impact of multi-path interference in high-speed scenarios.

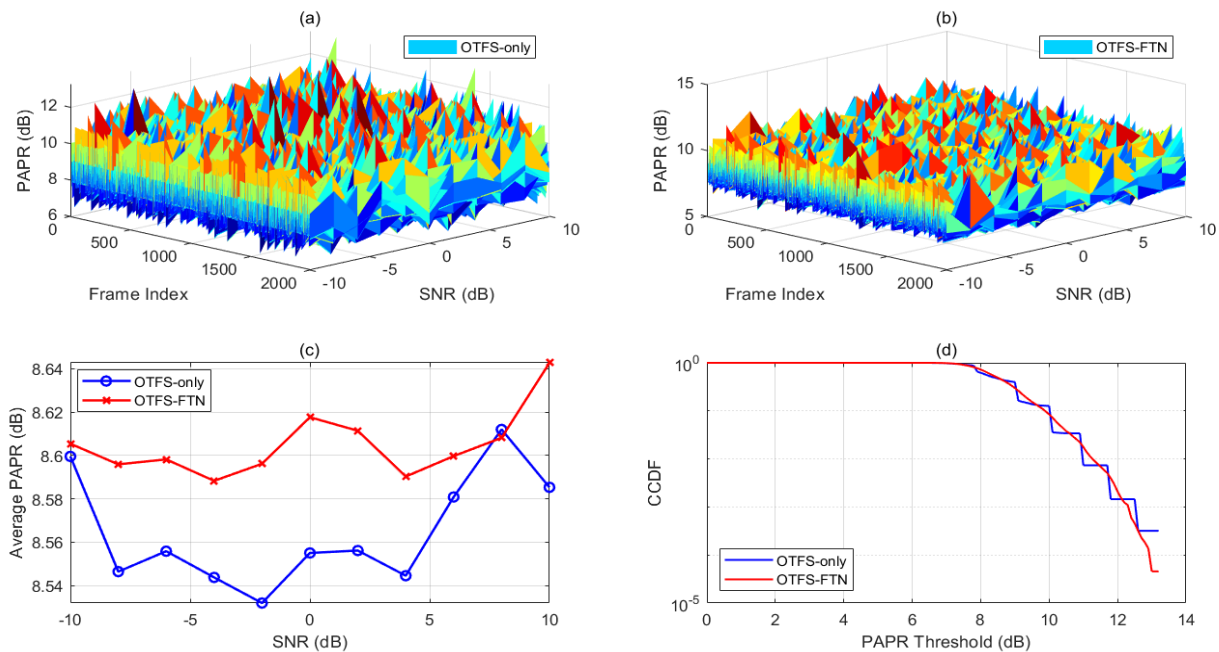


Fig. 4. PAPR (a & b) and CCDF (c & d) of the OTFS-FTN and OTFS schemes with $\alpha = 0.8$, $M = 32$ and $N = 32$.

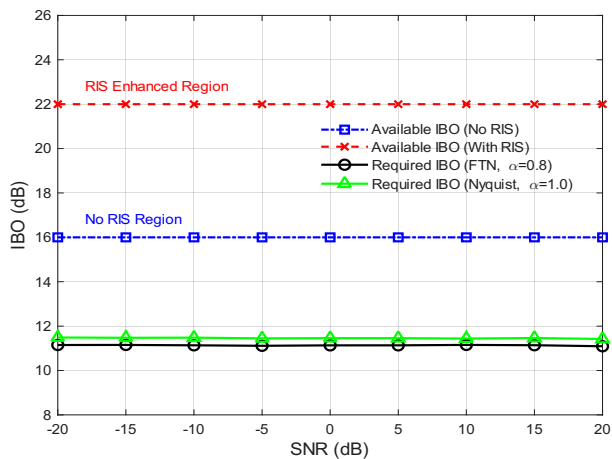


Fig. 5. IBO of the RIS-OTFS-FTN and OTFS-FTN schemes with $\alpha = 0.8$ and 1, $M = 32$ and $N = 32$.

exists no direct vehicle-user channel, with the RIS positioned equidistantly from both the vehicle and the user.

Fig. 4 compares the PAPR characteristics of the proposed RIS-OTFS-FTN scheme with those of the conventional OTFS scheme. Note that the RIS is not considered in this figure since the PAPR is only evaluated the transmitted signals, so Q can be ignored here and the legend of our scheme in Fig. 4 is simplified as the OTFS-FTN. The results reveal that the FTN-based scheme exhibits a PAPR distribution closely matching that of the Nyquist-based OTFS counterpart, indicating that for the current parameter settings, the application of FTN exerts an acceptable influence on the overall PAPR behavior. (c) and (d) of Fig. 4 present the CCDF of the PAPR for both schemes. The two CCDF curves almost completely overlap, demonstrating that the FTN-enabled scheme yields negligible

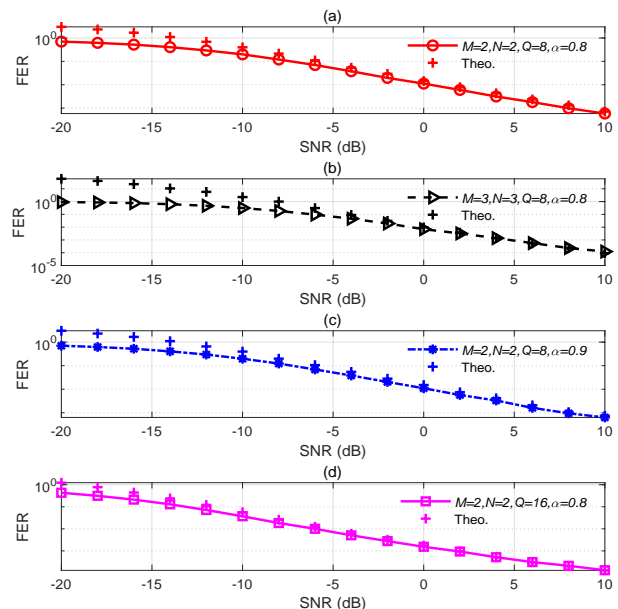


Fig. 6. Small-scale theoretical and simulation FER of the RIS-OTFS-FTN scheme with different M , N , Q , and α .

PAPR penalty compared to conventional OTFS. In the PAPR range of approximately 8–12 dB, the red curve (FTN) is slightly shifted to the right and lies marginally above the blue curve (OTFS), with minor fluctuations in some segments. This behavior indicates that FTN marginally increases the probability of higher PAPR occurrences in the tail region, although the increase is minimal. From a practical perspective, the observed PAPR behavior implies that the spectral efficiency advantages of FTN can be leveraged without incurring significant PAPR-related drawbacks. Moreover, as later illustrated in Fig. 4, the deployment of RIS compensates for even this small PAPR

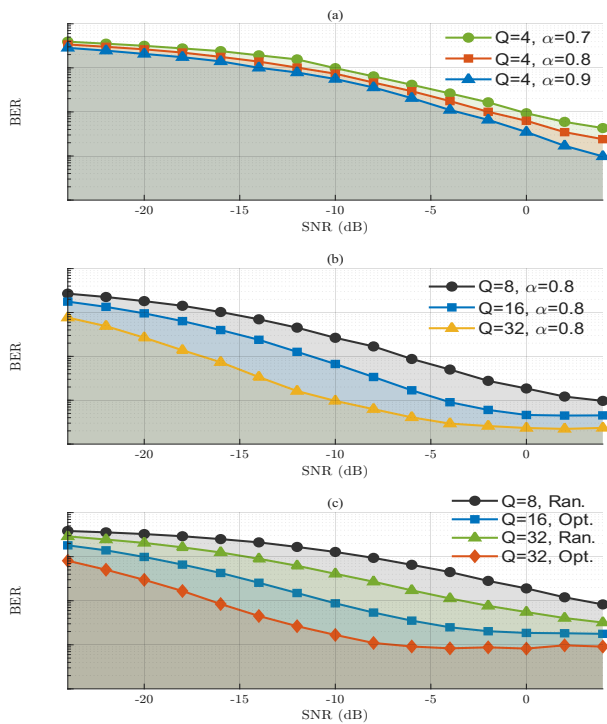


Fig. 7. BER of the MMSE detector-assisted RIS-OTFS-FTN scheme with various comparing cases: (a) $Q = 4$ and $\alpha = 0.7, 0.8, 0.9$; (b) $\alpha = 0.8$ and $Q = 8, 16, 32$; (c) $\alpha = 0.8$, $Q = 8, 16, 32$ in optimal phase adjustment (Opt.) and the random phase one (Ran.).

rise by enhancing the effective channel gain, thereby enabling reduced transmit power while meeting the same quality-of-service constraints. Therefore, despite the minimal PAPR difference, the proposed RIS-OTFS-FTN scheme maintains clear advantages in spectral efficiency and energy efficiency in high-mobility EVA channel scenarios.

Fig. 5 illustrates the input back-off (IBO) performance of the proposed RIS-OTFS-FTN scheme compared to that of the OTFS-FTN scheme without RIS assistance. Notably, considering normal configuration in the RIS and better presentation, a fixed value of $G_{RIS} = 6$ dB is given here. Here, the available IBO is computed according to (44), where the PA saturation power is fixed and the average transmit power is determined based on E_f . As shown in the figure, the RIS-assisted scheme consistently achieves a higher available IBO across the entire SNR range, with the improvement becoming more pronounced at higher SNR values. This behavior is attributed to the additional channel gain introduced by the RIS, which enables the transmitter to operate at a lower average power for the same error performance, thereby increasing the linear margin⁵ between the average transmit power and the PA saturation limit. The results clearly demonstrate the energy-efficiency benefits of incorporating RIS in high-mobility OTFS-FTN systems. In particular, the increased available IBO relaxes

⁵linear margin refers to the margin of input signal dynamic range that a system or device can withstand while maintaining the linear characteristics of the output signal. To put it simply, it is the allowable fluctuation range of input power without causing significant nonlinear distortions (such as harmonics and inter-modulation interference). A larger margin indicates a stronger ability of the system to resist distortion when dealing with signal changes.

the linearity requirements of the PA, reduces the risk of nonlinear distortion, and allows for more efficient operation without compromising signal integrity. From a system design perspective, this implies that the RIS-OTFS-FTN scheme can maintain robust performance even when operating closer to the PA's nonlinear region, thus reducing hardware constraints and improving overall power efficiency. Moreover, the observed IBO advantage complements the PAPR analysis in Fig. 4, as the RIS gain not only offsets the minimal PAPR increase due to FTN but also extends the operational flexibility of the transmitter in practical deployments. Moreover, by comparing the results with Nyquist signaling baseline ($\alpha = 1$, i.e., without FTN) alongside the proposed FTN scheme ($\alpha = 0.8$), it is observed that the curve for FTN ($\alpha = 0.8$) is comparable to, and in some regions even marginally lower than, that of the Nyquist baseline. That is, the proposed scheme achieves higher spectral efficiency without incurring a penalty in terms of PAPR or linearity requirements.

For Fig. 6, the theoretical and simulation FER results are presented with a small-scale running in different M , N , and α , as given in figure.⁶ The simulation results are still under the assumption of cascaded channel gain \mathbf{H}_{eff} following the Rayleigh fading, and the RIS gain is also considered. In Fig. 6, we can observe that the theoretical upper bound on FER closely aligns with the simulation results, particularly at higher SNR values where $\text{SNR} \gg -5$. A slight divergence is observed at lower SNR, attributable to the looseness of the union bound in regimes dominated by noise. Comparing to (a), (c), and (d), (b) increases the grid size to $M = 3$, $N = 3$ while maintaining $Q = 8$ and $\alpha = 0.8$, revealing a marginal degradation in FER performance. This is expected, as larger grids introduce more symbols per frame, increasing susceptibility to ISI and channel impairments, though the theoretical curve continues to serve as a reliable upper bound. (c) examines the impact of a higher compression factor $\alpha = 0.9$ with $M = 2$, $N = 2$, and $Q = 8$, demonstrating improved FER relative to $\alpha = 0.8$ in (a). The reduced FTN compression mitigates ISI, leading to lower error rates, with the theoretical and simulated curves exhibiting strong agreement. Finally, (d) doubles the RIS elements to $Q = 16$ while keeping $M = 2$, $N = 2$, and $\alpha = 0.8$, yielding a notable enhancement in FER performance over (a). The additional RIS elements provide greater received SNR, effectively strengthening the cascaded channel and reducing error probabilities, as corroborated by the tighter alignment between theory and simulation.

Fig. 7 illustrates the BER performance of the MMSE detector-assisted RIS-OTFS-FTN scheme across same values of $M = 16$ and $N = 16$ and various configurations in Q and α , as given in title. Note that the Opt. and Ran. in legends represent the optimal RIS phase design in this paper and random phase selection, respectively. In (a), with a fixed number of RIS elements $L = 4$ and different $\alpha = 0.7, 0.8, 0.9$,

⁶The use of small-scale grids (e.g., $M, N \leq 3$) in these evaluations is necessitated, due to the extremely large computational complexity of constructing and evaluating all possible symbol combinations and ergodic calculation in the ML detector. This renders full-scale simulations infeasible within reasonable computational resources, motivating the focus on small-scale scenarios to validate the analytical framework while providing insights scalable to practical systems.

the BER decreases as α increases, approaching the Nyquist signaling regime ($\alpha = 1$). This is also because higher α values reduce the severity of intentional ISI introduced by FTN, leading to improved detection accuracy. However, the differences in BER among these α values are relatively approached, particularly at low-to-moderate SNR, indicating that the spectral efficiency gains from lower α come at a limited cost in error performance under the MMSE detector. (b) examines the impact of increasing reflection elements in the RIS ($L = 8, 16, 32$) with fixed $\alpha = 0.8$. As Q increasing, the BER performance improves significantly due to enhanced channel gain through the RIS. Notably, an error floor trend emerges at higher SNR, becoming more pronounced and appearing earlier at lower SNR with larger Q . This behavior is attributed to the increased ISI in the cascaded vehicle-RIS-user channels, where more reflection elements amplify multi-path components, exacerbating interference in the DD domain and limiting the MMSE detector's ability to fully mitigate it. **For (c), the Ran. design yields substantially higher BER across all SNR by comparing to the Opt. design with differences exceeding an order of magnitude in some regions, especially with high Q and in low SNR range.** This underscores the critical role of Algorithm 1, which aligns reflected signals constructively to maximize channel gain.

Fig. 8 depicts the BER performance of the RIS-OTFS-FTN scheme with MMSE detector in comparison to benchmark variants, including schemes without RIS or FTN, as well as different α M and N ., as shown in figure. Notably, the RIS-OTFS scheme ($\alpha = 1$) achieves superior performance relative to FTN-enabled variants at equivalent grid sizes, attributable to its use of ideal rectangular pulses rather than the RRC filter employed in FTN processing. And the RIS-OTFS-FTN with $M = 16$, $N = 16$, $Q = 8$, and $\alpha = 0.8$ extremely outperforms the OTFS-FTN without RIS, demonstrating that RIS can better enhance the effective channel strength and mitigates fading in high-mobility scenarios. Similarly, comparing RIS-OTFS-FTN to RIS-OTFS, FTN variant introduces additional ISI due to time-domain compression, leading to a performance degradation, particularly evident at higher SNR where an error floor emerges, which is because increased grid dimensions amplify the impact of residual ISI and channel dispersion in the DD domain, limiting MMSE detector's equalization capability. Besides, the BER performance improves as M and N increases, which happens because larger OTFS grids offer finer resolution in the DD domain, enabling better exploitation of channel diversity and more effective equalization of multi-path and Doppler effects in detection. **For the results with message passing (MP) detector, which has 100 maximum number of MP detector iterations and damping parameter $\omega_{MP} = 0.8$, we observe that despite the dense channel graph, the MP detector's ability to explicitly model the FTN interference structure allows it to outperform LMMSE in the high-SNR regime, effectively improving the error performance in high SNR range. This confirms that while MP is computationally expensive in RIS environments, it is necessary for maximizing reliability when aggressive FTN compression is applied.**

Fig. 9 evaluates the spectral efficiency of the RIS-OTFS-FTN scheme under various configurations, including same

$Q = 32$, different α , M , and N , as given in title and legend of figure. In (a), with fixed $M = 16$ and $N = 16$, the spectral efficiency is compared for $\alpha = 1, 0.9, 0.8, 0.7$ across $Q = 30, 20, 10, 0$. As α decreases, the spectral efficiency exhibits a significant increase, consistent with the inverse proportionality to α in the normalization factor of (40). This enhancement stems from FTN's ability to pack more symbols within the same frame duration, as illustrated in Fig. 3. Notably, as shown in Fig. 8, while lower α values degrade BER due to heightened ISI, the spectral efficiency gains are substantial and continue to grow with diminishing α , highlighting a clear trade-off between error performance and throughput. Furthermore, increasing Q amplifies the spectral efficiency across all α , attributable to the RIS-induced boost in effective channel gain, particularly at higher SNR where the scheme approaches capacity. (b) fixes $Q = 10$ and varies $\alpha = 1, 0.9, 0.8, 0.7$ with $M = N = 8, 16, 32$. Similar to (a), spectral efficiency increases with decreasing α , reinforcing FTN's efficiency benefits. Intriguingly, smaller grid sizes in MN yield higher spectral efficiency, as the normalization in (40) scales inversely with MN , implying that compact frames benefit more from FTN compression relative to the occupied time-frequency resources. In summary, the RIS-OTFS-FTN scheme embodies a strategic trade-off in high-mobility wireless environments: FTN enhances SE at the cost of BER degradation, RIS scaling bolsters both reliability and efficiency, and grid sizing influences the normalized performance. By considering these effects, the proposed framework offers a versatile alternative to conventional OTFS, adaptable to diverse scenarios such as spectrum-constrained urban vehicular networks or energy-limited high-speed links, thereby providing an additional tool to combat challenging propagation conditions.

Fig. 10 depicts the BER performance under imperfect CSI with varying estimation error variances $\sigma_e^2 \in \{0, 0.1, 0.2\}$, and investigates the impact of finite phase resolution on the BER performance. It is observed that while the performance naturally degrades as the estimation accuracy decreases, the system does not suffer from catastrophic failure. Even with a relatively large error variance of $\sigma_e^2 = 0.2$, the proposed RIS phase alignment strategy maintains a valid gain, exhibiting a graceful performance degradation. This confirms the robustness of the proposed scheme against system uncertainties in high-mobility scenarios. (b) evaluates the impact of phase quantization resolution $B \in \{1, 2, 3\}$ bits compared to the ideal continuous phase case. The results demonstrate that the performance gap between the $B = 3$ bits quantization and the continuous phase is negligible. Also, the $B = 2$ bits configuration incurs only a marginal SNR penalty, approximately 1-2 dB at $\text{BER} = 10^{-2}$, while significantly reducing hardware complexity. However, the 1-bit quantization results in a noticeable performance loss due to the large phase mismatch. These results indicate that a low-resolution RIS architecture is sufficient to realize the benefits of the proposed RIS-OTFS-FTN scheme, making it a cost-effective solution for practical deployment.

Fig. 11 illustrates the BER performance as a function of user velocity ranging from 0 to 6000 km/h, with a fixed high SNR of 20 dB to isolate the impact of Doppler-induced impairments. The "operating limit" is defined as the maximum

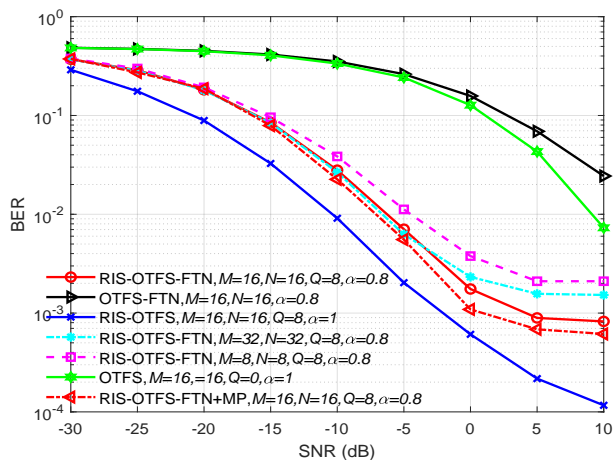


Fig. 8. BER of the RIS-OTFS-FTN scheme with/without RIS, FTN, MP detector, as well different M and N .

velocity. For the configuration with $M = N = 16$ and $Q = 16$, the system exhibits robust performance up to approximately 1,700 km/h. This indicates that for standard high-speed vehicular or railway scenarios (< 500 km/h), the proposed scheme operates well within its safety margin with negligible Doppler-induced degradation. Increasing the OTFS grid size to $M = N = 32$ significantly extends the tolerance limit to roughly 2,800 km/h. The finer resolution in the Delay-Doppler domain allows for more accurate channel resolvability and effective separation of high-Doppler paths. Further increasing the number of RIS elements to $Q = 32$ pushes the operating limit beyond 4,800 km/h. The enhanced passive beamforming gain provided by the larger RIS array effectively compensates for the SNR degradation caused by severe inter-carrier interference at hypersonic speeds. Increasing the OTFS grid size to $M = N = 32$ significantly extends the tolerance limit to roughly 2,800 km/h. Besides, A larger N reduces the Doppler bin spacing ($\Delta\nu = \frac{1}{NT}$), enabling the receiver to resolve closely spaced high-Doppler paths that would otherwise merge or cause severe inter-carrier interference (ICI) in a coarser grid, which is why the BER gets better with increase of MN . In summary, the proposed architecture demonstrates exceptional robustness, making it a viable candidate not only for terrestrial high-mobility networks but also for future non-terrestrial networks (NTN) such as LEO satellite communications.

VI. CONCLUSION

This study has established a comprehensive theoretical framework for the RIS-assisted OTFS-FTN paradigm in next-generation high-mobility wireless ecosystems. Closed-form expressions for AFER, spectral efficiency, PAPR, and IBO have been rigorously derived and extensively validated through abundant Monte-Carlo simulations, offering deeper insights into the interplay among FTN compression, OTFS modulation, and RIS applications. Furthermore, a capacity-maximizing RIS phase-optimization algorithm that constructively aligns the cascaded DD channel has been devised at the receiver. The synergistic exploitation of RIS, OTFS, and FTN has

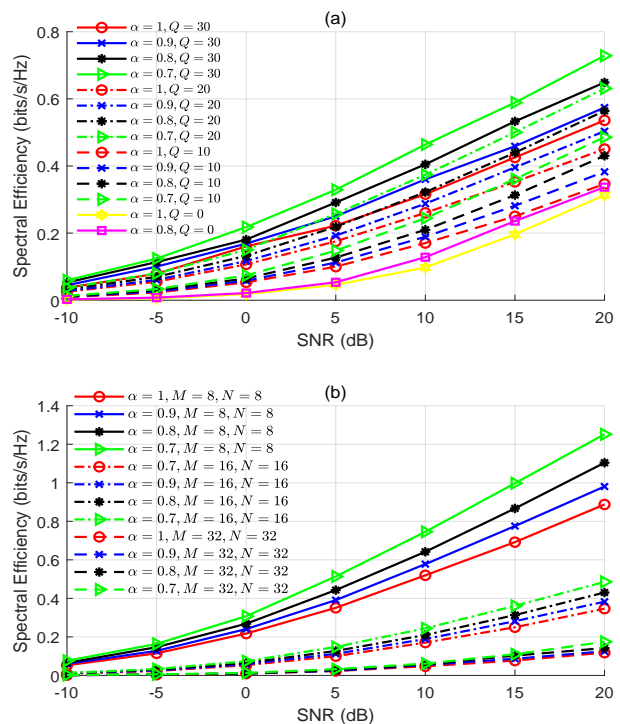


Fig. 9. Spectral efficiency of the RIS-OTFS-FTN scheme with different cases in (a) $\alpha = 1, 0.9, 0.8, 0.7, Q = 30, 20, 10, 0, M = 16$, and $N = 16$; (b) $\alpha = 1, 0.9, 0.8, 0.7, Q = 10, M = 8, 16, 32$, and $N = 8, 16, 32$.

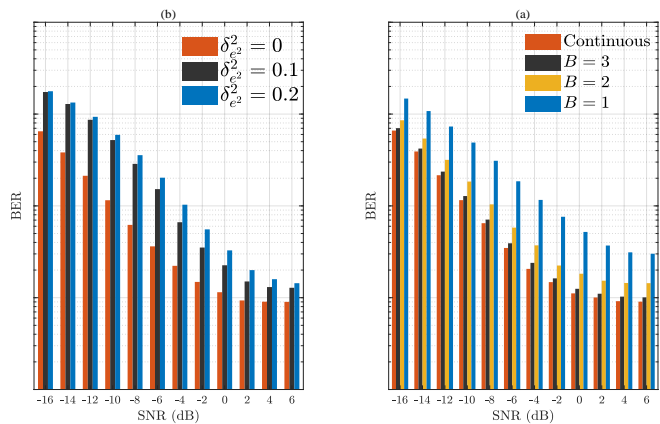


Fig. 10. BER of the RIS-OTFS-FTN scheme with imperfect CSI in different δ_c^2 and varying number of quantized adjusted phases B .

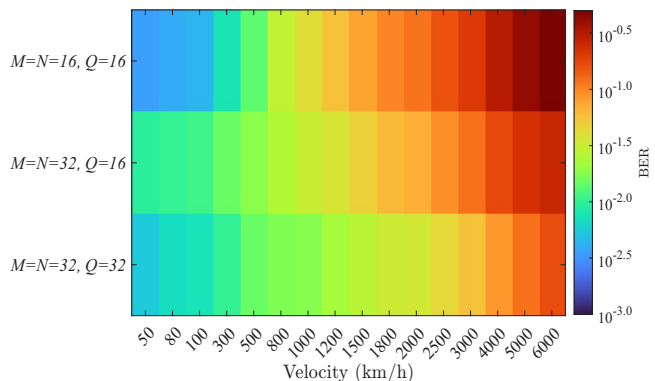


Fig. 11. Operating limits analysis of the RIS-FTN-OTFS: BER versus User Velocity (km/h) at SNR = 20 dB.

demonstrated substantial enhancements in spectral and energy efficiency while preserving robust error performance under realistic EVA channels. It should be emphasized that, when it comes to practical deployment, the trade-off among α , grid size $M \times N$, and L needs to be carefully balanced. As an optional scheme, the RIS-OTFS-FTN framework is proven to have great potential for future vehicular, railway, and satellite networks that demand high throughput under severe Doppler and blockage conditions.

REFERENCES

- [1] Q. Deng, Y. Ge, and Z. Ding, "A unifying view of OTFS and its many variants," *IEEE Commun. Surveys Tuts.*, vol. 27, no. 6, pp. 3561–3586, Dec. 2025.
- [2] M. Zhang *et al.*, "Fractional delay and Doppler estimation for OTFS systems with Doppler squint effect," in *Proc. IEEE Wireless Commun. Netw. Conf. (WCNC)*, Milan, Italy, 2025, pp. 1–6.
- [3] M. Aldababsa, *et al.*, "A survey on orthogonal time frequency space modulation," *IEEE Open J. Commun. Soc.*, vol. 5, pp. 4483–4518, 2024.
- [4] L. Gaudio, G. Colavolpe, and G. Caire, "OTFS vs. OFDM in the presence of sparsity: A fair comparison," *IEEE Trans. Wireless Commun.*, vol. 21, no. 6, pp. 4410–4423, Jun. 2022.
- [5] Z. Zhou, L. Liu, J. Xu, and R. Calderbank, "Learning to equalize OTFS," *IEEE Trans. Wireless Commun.*, vol. 21, no. 9, pp. 7723–7736, Sep. 2022.
- [6] R. Hadani *et al.*, "Orthogonal time frequency space modulation," in *Proc. IEEE Wireless Commun. Netw. Conf. (WCNC)*, San Francisco, CA, USA, 2017, pp. 1–6.
- [7] W. Yuan *et al.*, "New delay Doppler communication paradigm in 6G era: A survey of orthogonal time frequency space (OTFS)," *China Commun.*, vol. 20, no. 6, pp. 1–25, Jun. 2023.
- [8] X. Zhou *et al.*, "Active terminal identification, channel estimation, and signal detection for grant-free NOMA-OTFS in LEO satellite Internet-of-Things," *IEEE Trans. Wireless Commun.*, vol. 22, no. 4, pp. 2847–2866, Apr. 2023.
- [9] Z. Zhang, M. Yuksel, and H. Yanikomeroglu, "Faster-than-Nyquist signaling for MIMO communications," *IEEE Trans. Wireless Commun.*, vol. 22, no. 4, pp. 2379–2392, Apr. 2023.
- [10] A. D. Liveris and C. N. Georghiadis, "Exploiting faster-than-Nyquist signaling," *IEEE Trans. Commun.*, vol. 51, no. 9, pp. 1502–1511, Sep. 2003.
- [11] H. Xu, C. Zhang, Q. Wu, B. K. Ng, C.-T. Lam, and H. Yanikomeroglu, "FTN-assisted SWIPT-NOMA design for IoT wireless networks: A paradigm in wireless efficiency and energy utilization," *IEEE Sensors J.*, vol. 25, no. 4, pp. 7431–7444, Feb. 2025.
- [12] M. Kulhandjian, E. Bedeer, H. Kulhandjian, C. D'Amours, and H. Yanikomeroglu, "Low-complexity detection for faster-than-Nyquist signaling based on probabilistic data association," *IEEE Commun. Lett.*, vol. 24, no. 4, pp. 762–766, Apr. 2020.
- [13] T. Bacchielli, L. Pucci, E. Paolini, and A. Giorgetti, "A low-complexity detector for OTFS-based sensing," *IEEE Trans. Wireless Commun.*, vol. 24, no. 6, pp. 5227–5240, Jun. 2025.
- [14] Z. Zhang, M. Yuksel, G. M. Guvensen, and H. Yanikomeroglu, "Capacity and IAPR analysis for MIMO faster-than-Nyquist signaling with high acceleration rate," *IEEE Trans. Wireless Commun.*, vol. 25, pp. 1451–1466, 2026.
- [15] M.-S. Baek, E.-S. Jung, Y. S. Park, and Y.-T. Lee, "FTN-based non-orthogonal signal detection technique with machine learning in quasi-static multipath channel," *IEEE Trans. Broadcast.*, vol. 70, no. 1, pp. 78–86, Mar. 2024.
- [16] H. Yang, *et al.*, "Frequency diverse array-enabled RIS-aided integrated sensing and communication," *IEEE Trans. Wireless Commun.*, vol. 24, no. 9, pp. 7546–7562, Sep. 2025.
- [17] C. Pan *et al.*, "An overview of signal processing techniques for RIS/IRS-aided wireless systems," *IEEE J. Sel. Topics Signal Process.*, vol. 16, no. 5, pp. 883–917, Aug. 2022.
- [18] K. Wang, C.-T. Lam, B. K. Ng, and Y. Liu, "On the impact of phase errors in phase-dependent amplitudes of near-field RISs," *IEEE Trans. Veh. Technol.*, Dec., 2025, early access.
- [19] C. Zhang, Y. Liu, B. K. Ng, and C.-T. Lam, "RIS-assisted differential transmitted spatial modulation design," *Signal Process.*, vol. 230, p. 109767, 2025.
- [20] K. Wang, R. Chen, C.-T. Lam, B. K. Ng, and C. Zhang, "How phase errors influence phase-dependent amplitudes in near-field RISs?," in *Proc. IEEE Veh. Technol. Conf. (VTC2024-Fall)*, Washington, DC, USA, 2024, pp. 1–6.
- [21] G. Harshavardhan, V. S. Bhat, and A. Chockalingam, "RIS-aided OTFS modulation in high-Doppler channels," in *Proc. IEEE 33rd Annu. Int. Symp. Pers. Indoor Mobile Radio Commun. (PIMRC)*, Kyoto, Japan, 2022, pp. 409–415.
- [22] A. Thomas, K. Deka, S. Sharma, and N. Rajamohan, "IRS-assisted OTFS system: Design and analysis," *IEEE Trans. Veh. Technol.*, vol. 72, no. 3, pp. 3345–3358, Mar. 2023.
- [23] Z. Li, W. Yuan, B. Li, J. Wu, C. You, and F. Meng, "Reconfigurable-intelligent-surface-aided OTFS: Transmission scheme and channel estimation," *IEEE Internet Things J.*, vol. 10, no. 22, pp. 19518–19532, Nov. 2023.
- [24] A. S. Bora, K. T. Phan, and Y. Hong, "IRS-assisted high mobility communications using OTFS modulation," *IEEE Wireless Commun. Lett.*, vol. 12, no. 2, pp. 376–380, Feb. 2023.
- [25] C. Xu *et al.*, "OTFS-aided RIS-assisted SAGIN systems outperform their OFDM counterparts in doubly selective high-Doppler scenarios," *IEEE Internet Things J.*, vol. 10, no. 1, pp. 682–703, Jan. 2023.
- [26] V. S. Bhat and A. Chockalingam, "RIS-aided OTFS with index modulation," in *Proc. IEEE Wireless Commun. Netw. Conf. (WCNC)*, Dubai, United Arab Emirates, 2024, pp. 1–6.
- [27] Z. Hong, S. Sugiura, C. Xu, and L. Hanzo, "Precoded faster-than-Nyquist signaling for OTFS," *IEEE Wireless Commun. Lett.*, vol. 14, no. 1, pp. 173–177, Jan. 2025.
- [28] M. Tong, X. Huang, J. Andrew Zhang, and L. Hanzo, "Adaptive FTN signaling over rapidly-fading channels," *IEEE Trans. Commun.*, vol. 73, no. 9, pp. 7166–7178, Sep. 2025.
- [29] X. Wang, S. Gong, W. Shen, C. Xing, and J. A. Zhang, "Multi-carrier faster-than-Nyquist signaling for OTFS systems," *IEEE Trans. Veh. Technol.*, vol. 74, no. 12, pp. 19339–19354, Dec. 2025.
- [30] H. Xu, C. Zhang, Q. Wu, B. K. Ng, and C.-T. Lam, "Adaptive damping log-domain message-passing algorithm for FTN-OTFS in V2X communications," *Sensors*, vol. 25, no. 12, p. 3692, Jun. 2025.
- [31] Z. Hong and S. Sugiura, "Reduced-complexity MIMO faster-than-Nyquist signaling transceiver for OTFS modulation," *IEEE Open J. Commun. Soc.*, vol. 6, pp. 6126–6141, 2025.
- [32] T. Thaj and E. Viterbo, "Low complexity iterative rake decision feedback equalizer for zero-padded OTFS systems," *IEEE Trans. Veh. Technol.*, vol. 69, no. 12, pp. 15606–15622, Dec. 2020.
- [33] M. K. Simon and M.-S. Alouini, *Digital Communication over Fading Channels*, 2nd ed. Wiley, 2005.
- [34] J. G. Proakis and M. Salehi, *Digital Communications*, 5th ed. McGraw-Hill, 2008.
- [35] G. D. Surabhi, R. M. Augustine, and A. Chockalingam, "Peak-to-average power ratio of OTFS modulation," *IEEE Commun. Lett.*, vol. 23, no. 6, pp. 999–1002, Jun. 2019.
- [36] 3GPP TS 36.101, "Evolved Universal Terrestrial Radio Access (E-UTRA); User Equipment (UE) radio transmission and reception," 3GPP, 2023.